Available online at www.sciencedirect.com

ScienceDirect

Geochimica et Cosmochimica Acta 132 (2014) 311–336

Geochimica et Cosmochimica Acta

www.elsevier.com/locate/gca

Melting of continental crust during subduction initiation: A case study from the Chaidanuo peraluminous granite in the North Qilian suture zone

Yuxiao Chen [a], Shuguang Song [a,*], Yaoling Niu [b,c], Chunjing Wei [a]

[a] MOE Key Laboratory of Orogenic Belts and Crustal Evolution, School of Earth and Space Sciences, Peking University, Beijing 100871, China
[b] Department of Earth Sciences, University of Durham, Durham DH1 3LE, UK
[c] Institute of Oceanonology, Chinese Academy of Science, Qingdao 266071, China

Received 9 August 2013; accepted in revised form 8 February 2014; Available online 26 February 2014

Abstract

The Chaidanuo granite batholith is a ~500 km^2 homogeneous, high-level intrusion in the North Qilian oceanic suture zone. Three types of enclaves have been recognized, including (1) supracrustal xenoliths, (2) biotite gneiss that represents restite of the upper crustal melting, and (3) coeval mantle-derived mafic magmatic enclave (MME). The batholith consists dominantly of peraluminous biotite monzogranite with SiO_2 69–73 wt.% and A/CNK 1.05–1.28 and shows geochemical affinity with the upper-continental crust, e.g., enrichment of large ion lithophile elements (LILEs; K, Rb, U, Th, Pb), depletion of high field strength elements (HFSEs; Nb, Ta, Ti), P, Eu, and Sr, and enriched Sr ($[^{87}Sr/^{86}Sr]_i$, 0.731 to 0.744)–Nd (ε_{Nd} (t), −6.0 to −7.1) isotopes. Zircon U–Pb dating indicates that this batholith formed at 516–505 Ma, coeval with the MMEs (510 Ma), which represent the early stage of seafloor subduction in the North Qilian suture zone. The Hf isotopic composition of the MME (εHf (t) = −6.0 to +2.1) is more depleted than that of the host granite (εHf (t) = −14.8 to −4.7), suggesting mixing of mantle- and crust-derived melts. The inherited zircon cores in the host granite yield an age peak at ~750 Ma with a few detritals of 591–1683 Ma. Zircons from a biotite gneiss enclave yield a protolith age of 744 Ma and a metamorphic/melting event at 503 Ma. Sr–Nd isotopic modeling reveals that the batholith was generated by melting of Neoproterozoic granitic rocks with the addition of 10–18% mantle-derived magma. Therefore, peraluminous granite can be produced by melting of crustal materials heated by mantle-derived magmas during the early stage of subduction initiation at the site of a prior passive continental margin.

1. INTRODUCTION

Peraluminous granitoids are universal in orogenic belts and can provide important clues for the growth and reworking/recycling of continental crust. Many studies have been devoted to a better understanding of their petrogenesis and tectonic setting by means of petrologic, geochemical and experimental investigations (McCulloch and Chappell, 1982; Chappell and Simpson, 1984; Miller, 1985; Chen et al., 1990; Vielzeuf and Montel, 1994; Gardien et al., 1995; Barbarin, 1996, 1999; Keay et al., 1997; Montel and Vielzeuf, 1997; Collins, 1998; Patiño Douce and Harris, 1998; Patiño Douce, 1999; Chappell and White, 2001; Clemens, 2003; Healy et al., 2004). Peraluminous granitoids are commonly considered as a result of anatexis of pure meta-sedimentary rocks during crustal thickening in response to orogenesis or some types of regional extension. Type examples include peraluminous granitoids (also named "leucogranite") in the Himalayan orogenic belt

* Corresponding author. Tel.: +86 10 62767729.
E-mail address: sgsong@pku.edu.cn (S. Song).

http://dx.doi.org/10.1016/j.gca.2014.02.011
0016-7037/

(Inger and Harris, 1993; Barbarin, 1996; Harrison et al., 1997; Patiño Douce and Harris, 1998; Sylvester, 1998; Patiño Douce, 1999) and the Massif Central in the Hercynian Belt (e.g., Williamson et al., 1996). Detailed studies in the Lachlan S-type granites (Chappell and White, 1974, 2001; McCulloch and Chappell, 1982; Gray, 1984, 1990; Keay et al., 1997; Collins, 1998, 2002; Healy et al., 2004) and the Cordilleran peraluminous granites (Ague and Brimhall, 1987; Shaw et al., 2003; Lucassen et al., 2004; Gaschnig et al., 2011) show that peraluminous granitoids can also form in subduction-related environments. Compared with collision-related peraluminous granitoids, subduction-related equivalents generally exhibit higher FeO, MgO, a wider range of SiO_2, more depleted isotopes than probable crustal source and usually have mafic magmatic enclaves (MMEs). The key question is whether these signatures reflect the contribution of mantle materials (e.g., Collins, 1998; Healy et al., 2004) or result from ineffective separation of restites (restite-unmixing model; e.g., Chappell and Wyborn, 2012).

Diverse natural examples and complex geological settings/histories make investigation of geodynamic implications of subduction-related peraluminous granitoids difficult, thereby various models had been proposed (Collins, 2002; Collins and Richards, 2008; Cai et al., 2011). Collins and co-authors emphasized that injection of mantle-derived basaltic magma into arc crust associated with long-term, repeated trench rollback and extension of back-arc basin afterwards can trigger melting of preexisting sediments deposited in the back-arc basin to form subduction-related peraluminous granitoids in the circum-Pacific subduction zone (Collins, 2002; Collins and Richards, 2008). Recently, Cai et al. (2011) interpreted that peraluminous granitoids in the Chinese Altai represent mixed melts derived from both subducted metasediments and mantle-derived melts related to ridge subduction. Based on petrological-thermomechanical modeling, Gorczyk et al. (2007) suggested that the late Paleozoic peraluminous granitoids in central Chile reported by Lucassen et al. (2004) are the consequence of local heating of continental crust by upwelling mantle at the boundary between the accretionary prism and continent in the nascent subduction. While this suggestion is interesting, more work is needed to actually understand the formation mechanism of peraluminous granitoids during subduction initiation.

The North Qilian orogenic belt at the northern margin of the Tibetan Plateau is a type Early Paleozoic suture zone and composed of subduction accretionary complexes including ophiolites, high-pressure/low-temperature (HP/LT) metamorphic rocks, arc volcanic and plutonic rocks, Silurian flysch formation, Devonian molasse, and post-Devonian sedimentary cover (see in details in the review paper by Song et al., 2013 and references there in). The Chaidanuo pluton is a large and fairly homogeneous high-level peraluminous intrusion, and offers an exceptional opportunity to study the petrogenesis of peraluminous granitoids associated with seafloor subduction. Wu et al. (2006a, 2010) reported a zircon SHRIMP age of 508 ± 5 Ma from a biotite monzogranite (Fig. 1) and interpreted the Chaidanuo batholith as sourced from Early Proterozoic sediments based on whole-rock geochemical data. In this paper, we present the results of a comprehensive study of the Chaidanuo peraluminous granitoids and relevant enclaves by integrating petrology, whole-rock major- and trace-element analyses, zircon U–Pb geochronology, and Hf isotope data as well as whole-rock Sr–Nd isotopic geochemistry. We suggest diapirism of mantle wedge and/or mantle-derived magmas during subduction initiation can trigger large-scale melting of the overriding continental crust.

2. GEOLOGICAL SETTING AND PETROGRAPHY

The northwest-trending North Qilian orogenic belt (NQOB) is located at the northeastern margin of the Tibet Plateau (Fig. 1). It extends for approximately 1000 km between the Alashan block (AB) to the north and the Qilian block (QB) to the south (for details, see Dan et al., 2012; Song et al., 2006, 2013), and is offset by the Altun Tagh fault, the largest sinistral-slip fault in northwestern China, to the west (e.g., Zhang et al., 2001).

The NQOB is an Early Paleozoic suture zone composed of three subunits, i.e., the southern ophiolite belt, the middle arc magmatic belt and the northern back-arc basin ophiolite-volcanic belt (Fig. 1a) (Xia et al., 2003, 2012; Xia and Song, 2010; Wu et al., 2011; Song et al., 2013). The southern ophiolite subbelt is composed of several ophiolite suites consisting of mantle peridotite, mafic–ultramafic cumulate, pillow basaltic lavas and radiolarian chert, which indicate seafloor spreading in the Qilian Ocean at ~560–500 Ma (Xiao et al., 1978; Shi et al., 2004; Tseng et al., 2007; Song et al., 2009b, 2013). The northern ophiolite-volcanic subbelt consists of ultramafic rocks, cumulates, basalts with N-type-MORB and island arc basalt (IAB) geochemical characteristics, as well as boninite with younger ages of ~490–449 Ma, suggesting extension of a back-arc basin associated with northward subduction in the Early Paleozoic (Zhang et al., 1998; Xia and Song, 2010; Xia et al., 2012; Song et al., 2006, 2009a,b, 2013). Between the two ophiolite subbelts is a subduction-related arc magmatic belt with three fault-bounded HP/LT metamorphic slices including eclogites and blueschists.

The arc magmatic subbelt is comprised of a boninite complex, an arc-volcanic complex and various calc-alkaline intermediate-felsic plutons. Neoproterozoic granitic gneisses (776–751 Ma) were reported in this subbelt (Su et al., 2004; Tseng et al., 2006, 2009). The boninite complex in the Dachadaban area is comprised of two distinct but successive lithological groups: a lower tholeiite unit and an upper boninite unit. This tholeiite-boninite sequence was interpreted to have been derived from continuous melting of a mantle wedge from subduction initiation at ~517 Ma to back-arc extension at ~487 Ma (Xia et al., 2012). The arc-volcanic complex is comprised predominantly of felsic (dacite to rhyolite) rocks with minor intermediate to mafic rocks formed at ~500–445 Ma (Zhang et al., 1997; Wang et al., 2005; Song et al., 2013). The granitic plutons were subdivided into volcanic arc granite (520–460 Ma), syn-collisional granite (440–420 Ma) and post-collision granite (<400 Ma) on the basis of their crystallization ages (Song

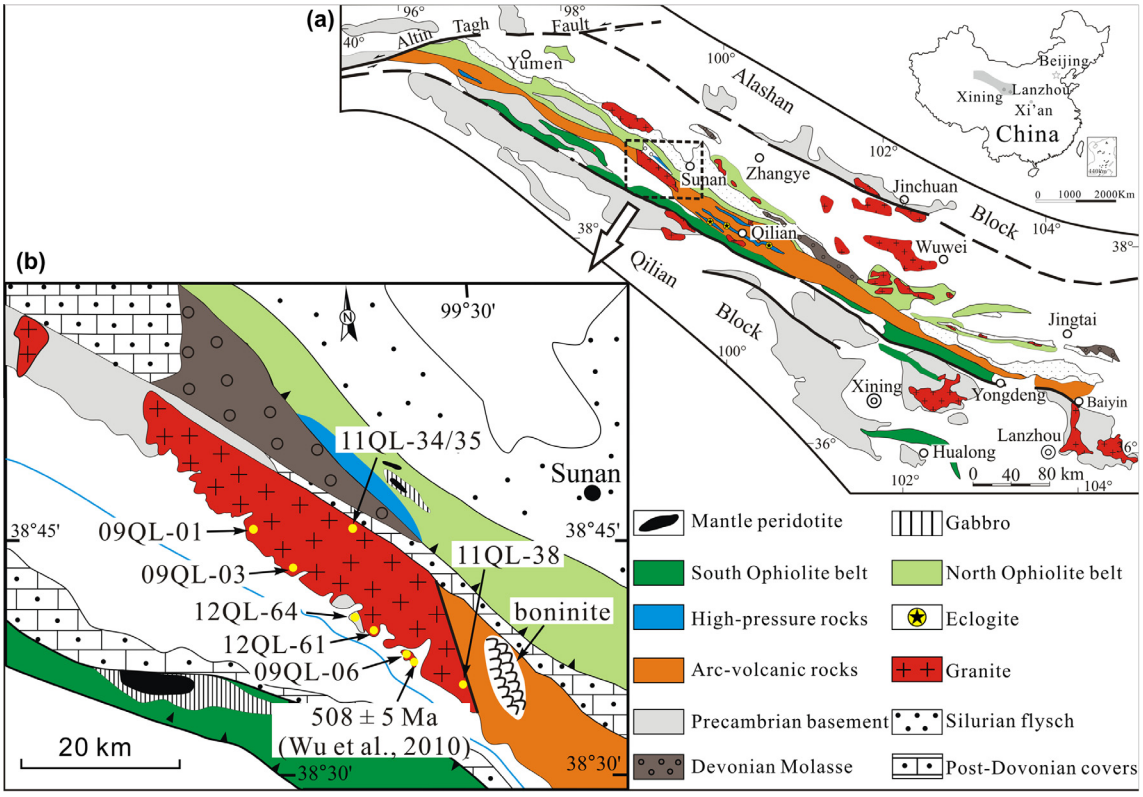

Fig. 1. Geological map of the North Qilian Orogen showing major tectonic units (a) and the Chaidanuo granitic batholith (b).

et al., 2013). All these subduction-related arc magmatic processes suggest that the Qilian Ocean may have initiated subducting beneath the Alashan block, as an Andean-type continental margin, no earlier than 520 Ma (Song et al., 2013).

The Chaidanuo granitic batholith is an elongated, 8–10 km wide, ~60 km long and ~500 km^2 NW-trending pluton along the arc magmatic belt. This batholith is cut by a ductile fault in the north, overlain by Cenozoic sediments in the south and intruded into a Precambrian volcanic-sedimentary complex and granitic gneisses (Fig. 1b). It is fairly homogeneous and can be readily distinguished in the field from other granitoids by its light color, weakly orientated fabrics and locally-preserved meta-sedimentary and meta-igneous enclaves near its margins (Fig. 2A–D).

The host granite is dominated by fine- to medium-grained locally porphyritic biotite monzogranite with a mineral assemblage of plagioclase (40–45%), K-feldspar (25–30%), quartz (~20–25%), biotite (~5%) and accessory minerals. Biotite is dark reddish brown in color, TiO_2-rich (2.89–3.35 wt.%) and strongly peraluminous in composition with molecular $Al_2O_3/(CaO + Na_2O + K_2O)$ ratios (Alumina Saturation index (ASI)) of 1.33–1.64 (Table 1). Most biotite crystals display "sagenitic texture", which refers to the presence of needle-like titanite inclusions intersecting at 60 angles (Fig. 2E). These inclusions are inferred to have precipitated from a parent solid solution during later cooling stage in the presence of excess Ti and Ca derived from biotite of igneous origin (Shau et al., 1991). Plagioclase is often sericitized with translucent cores surrounded by Na-rich, transparent rims of low An = 3–6% (Fig. 2F). K-feldspar often occurs as 1–5 mm anhedral grains occasionally with perthitic exsolution lamellae, and has biotite and plagioclase inclusions, reflecting its later crystallization. Accessory minerals include allanite, titanite, zircon, apatite, and ilmenite, where allanite occurs as euhedral crystals showing clear core-rim zoning.

Three types of enclaves are recognized in the host granite: (I) sedimentary-volcanic xenoliths, (II) mafic magmatic enclaves (MMEs), and (III) biotite gneisses and biotite aggregates.

Type I sedimentary-volcanic xenoliths occur locally in the outer edge of the pluton, probably being trapped from the top of the magma chamber. They are usually angular, of varied size (up to several tens of centimeters in diameter) and exhibit sharp contact with the host granite (Fig. 2C and D). This is consistent with xenoliths entrained from the country rocks in the upper crust, suggesting that the Chaidanuo granite is a high-level intrusion (Didier and Barbarin, 1991).

Type II MMEs are rounded, and mostly small in size of 1–10 cm across (Fig. 2G). They are composed of biotite, amphibole, plagioclase with minor quartz, and Fe–Ti oxide. Plagioclase is euhedral and amphibole is anhedral with a light-green to light-brown color. Some show clear reaction rims with the host granite, where red-brown biotite crystals cluster around the amphibole-bearing cores. These reflect the reaction of MMEs with the K-rich peraluminous melts.

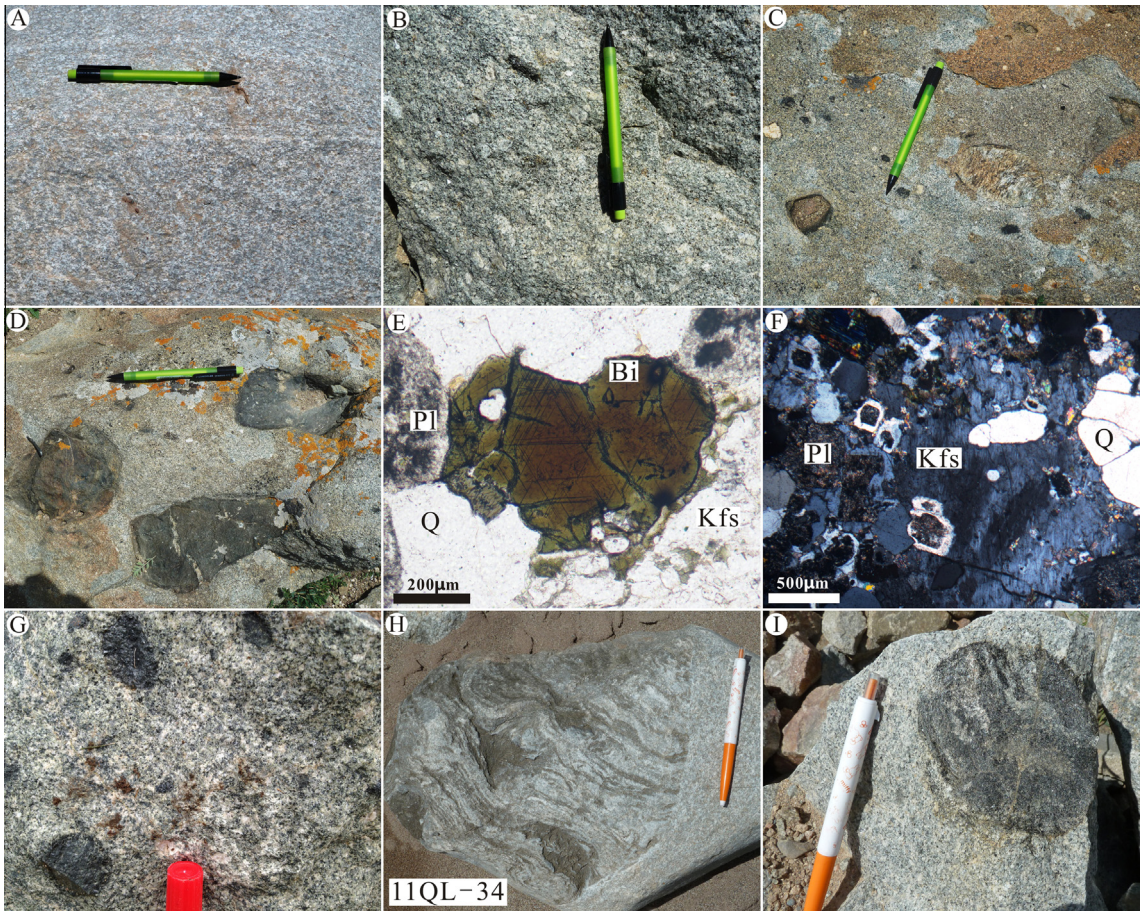

Fig. 2. Photographs showing the host granites and enclaves from the Chaidanuo batholith. (A) and (B) the host biotite monzogranite (sample 11QL-38); (C) various rock types of enclaves including meta-sedimentary and volcanic xenoliths; (D) volcanic xenoliths with variable shapes; (E) biotite in the host granite exhibiting needle-like inclusion at 60° angles; (F) plagioclase in the host granite having sericitized cores surrounded by Na-rich rims; (G) mafic magmatic enclaves (MMEs) with rounded shapes showing reaction relationship with the host granite; (H) the biotite gneiss enlave with strong foliation and biotite aggregates; (I) Biotite-rich clots.

Type III biotite gneiss enclaves are rare and occur as rounded blocks of 10–100 cm in diameter in the interior of the pluton (Fig. 2H). They resemble the host granite in mineral assemblage, but have variable and high modal content of red-brown biotite and some show strong deformation. Biotite crystals are also strongly peraluminous (ASI = 1.66–1.73), have higher FeO (22.38–22.98 wt.%) and Al_2O_3 (17.13–17.85 wt.%), but lower TiO_2 (1.51–1.66 wt.%) than those in the host granite (Table 1). They cluster along the foliation displaying the same "sagenitic texture" as biotites in the host granite (Table 1). Some enclaves are biotite aggregates with a few quartz and feldspar crystals (Fig. 2I).

3. ANALYTICAL METHODS

The bulk-rock major and trace elements were analyzed using Leeman Prodigy inductively coupled plasma-optical emission spectroscopy (ICP-OES) and Agilent-7500a inductively coupled plasma mass spectrometry (ICP-MS) at China University of Geosciences, Beijing, respectively. The analytic procedure and precisions are described by Song et al. (2010b) and the data are given in Table 2.

For Sr–Nd isotope analysis, 100–150 mg powders of four fresh host granite samples, one biotite gneiss enclave sample and BCR-2 standard were dissolved using $HClO_4$ and HF in Teflon vessels and Sr and Nd elements were acquired by further separation work in Peking University, Beijing. The analysis was done on a Triton Thermal Ionization Mass Spectrometer at the Institute of Geology and Mineral resources, Tianjin. Detailed procedure follows that of Jahn et al. (1996). During the course of this study, the mean $^{87}Sr/^{86}Sr$ ratios for NBS-987 and BCR-2 are 0.710238 ± 5 ($n = 3$) and 0.705016 ± 3 ($n = 2$), respectively, while the mean $^{143}Nd/^{144}Nd$ ratios are 0.512118 ± 6 ($n = 5$) for JNDI and 0.512637 ± 6 ($n = 2$) for BCR-2. Data are presented in Table 3.

Zircon separation was conducted in a laboratory of the Langfang Institute of Regional Geological Survey by initial heavy liquid and magnetic extraction followed by hand-picking under a binocular. The zircon grains were mounted in an epoxy disc that was then polished to expose zircon interiors. Cathodoluminescence (CL) images were obtained using a FEI PHILIPS XL30 SFEG Scanning Electron Microscope (SEM) with 3-min scanning

Table 1
Representative microprobe analyses of minerals.

Mineral	Sample#	SiO_2	TiO_2	Al_2O_3	FeO	MnO	MgO	CaO	Na_2O	K_2O	Cr_2O_3	Totals	ASI	Fe/(Fe + Mg)	An
Biotite	11QL-42	35.75	3.280	16.72	21.42	0.440	7.820	0.040	0.250	8.960	2.210	96.89	1.64	0.61	
	11QL-42	34.79	2.890	16.37	21.72	0.410	8.170	0.040	0.070	9.810	0.150	94.42	1.52	0.60	
	12QL-59	36.14	3.350	14.46	20.25	0.360	9.730	0.040	0.030	9.960	0.050	94.37	1.33	0.54	
	11QL-34	36.22	1.510	17.77	22.74	0.270	8.240	0.010	0.080	9.730	0.040	96.61	1.66	0.61	
	11QL-34	35.71	1.570	17.55	22.77	0.340	8.050	0.000	0.120	9.510	0.010	95.63	1.67	0.61	
	11QL-34	35.57	1.650	17.13	22.38	0.310	7.880	0.010	0.140	9.280	0.190	94.54	1.66	0.61	
	11QL-34	35.68	1.660	17.85	22.98	0.280	8.040	0.000	0.150	9.320	0.080	96.04	1.73	0.62	
K-feldspar	11QL-42	64.37	0.030	18.85	0.000	0.000	0.000	0.040	0.560	16.38	0.030	100.26			
	11QL-42	64.91	0.000	18.68	0.000	0.000	0.000	0.030	0.530	16.20	0.050	100.40			
	09QL-05	65.64	0.000	18.73	0.000	0.000	0.000	0.050	0.550	14.62	0.000	99.58			
	09QL-05	67.01	0.010	18.71	0.000	0.000	0.000	0.010	0.350	14.80	0.020	100.91			
	11QL-34	65.12	0.000	18.34	0.000	0.010	0.000	0.000	0.470	15.76	0.020	99.73			
	11QL-34	64.96	0.080	18.50	0.000	0.000	0.000	0.000	0.370	15.75	0.000	99.65			
	11QL-42	67.75	0.060	18.74	0.000	0.000	0.000	0.610	11.77	0.090	0.030	99.05			3
Plagioclase	09QL-05	67.13	0.040	20.80	0.000	0.000	0.040	1.300	10.69	0.420	0.000	100.43			6
	11QL-34	66.65	0.020	20.98	0.000	0.020	0.000	2.050	10.40	0.070	0.040	100.24			10
	11QL-34	68.97	0.070	19.54	0.000	0.000	0.000	0.590	11.03	0.070	0.000	100.26			3
Titanite inclusion in biotite	11QL-34	31.33	35.18	4.040	0.770	0.020	0.000	28.52	0.030	0.190	0.000	100.08			

Biotite gneiss enclave: 11QL-34; Host granite: 09QL-05, 11QL-42 and 12QL-59.

time in condition 15 kV/nA in the School of Earth and Space Science, Peking University, Beijing.

Measurement of U, Th and Pb in zircons were conducted using the Cameca IMS-1280 ion microprobe (CASIMS) at the Institute of Geology and Geophysics, Chinese Academy of Sciences in Beijing and the Agilient 7500a Q-ICP-MS equipped with a 193 nm laser housed at the Geologic Lab Center, China University of Geosciences, Beijing and Peking University. Operating conditions and data processing of CASIMS follow those described by Li et al. (2009). The analytical procedure of LA-ICP-MS is given in detail in Song et al. (2010a). The size of the analytic laser spot is ellipsoidal, about 20 × 30 μm for SIMS and circular, 36 × 36 μm for LA-ICP-MS. U–Pb isotope fractionation effects were corrected by using external standard zircon 91500 (Wiedenbeck et al., 1995) and a secondary standard zircon TEMORA (417 Ma) from Australia (Black et al., 2003). Sixteen spots for the standard TEMORA gave apparent $^{206}Pb/^{238}U$ ages of 415–418 Ma with a weighted mean of 417.1 ± 2.5 Ma (MSWD = 0.04). The $^{207}Pb/^{206}Pb$ and $^{206}Pb/^{238}U$ ratios were calculated based on the GLITTER program and Isoplot/Ex (3.0) (Ludwig, 2003). The common lead was corrected using LA-ICP-MS Common Lead Correction (ver. 3.15), followed the method of Andersen (2002). Individual analyses are presented with 1σ errors in data tables and in concordia diagrams. The uncertainties in mean ages are quoted at 95% level. Results are given in Tables 4 and 5.

In-situ zircon Hf isotopic analysis was done using a Neptune multi-collector ICP-MS, equipped with a Newwave UP213 laser in Tianjin Institute of Geology and Mineral resources and the MLR Key Laboratory of Metallogeny and Mineral Assessment, Institute of Mineral Resources, Chinese Academy of Geological Sciences (Beijing) following the standard operating procedure and data processing described by Hou et al. (2007) and Wu et al. (2006b). Zircon GJ1, the reference standard used in this study, yielded a weighted mean $^{176}Hf/^{177}Hf$ ratio of 0.282007 ± 0.000007 (2σ, $n = 15$), which is in good agreement with the recommended $^{176}Hf/^{177}Hf$ ratio of 0.282000 ± 0.000013 (2σ) using a solution analysis method by Morel et al. (2008). Results are given in Table 6.

4. RESULTS

4.1. Major and trace elements

Seventeen representative Chaidanuo granite samples and a biotite gneiss enclave were analyzed for whole-rock major and trace element compositions (Table 2). The localities of these analyzed samples cover the ~50 km length of the batholith from the northwest to southeast. The granite samples are characterized by high Al_2O_3 (12.98–14.64 wt.%), K_2O (4.00–5.58 wt.%) and K_2O/Na_2O ratios (1.3–3.9) and medium total alkaline concentrations ($Na_2O + K_2O$ = 5.75–9.21 wt.%), plotting predominantly in the granite field (Fig. 3a). All samples are peraluminous with ASI ratios ranging from 1.03 to 1.28 except for sample 10QL-101 (ASI = 0.97) (Fig. 3b). Normative corundum ranges from 1.19 to 3.14 wt.% except for sample 10QL-101. According to the geochemical classification of Frost et al. (2001), these granitic rocks are mainly magnesian and alkali-calcic to calcic-alkali. The biotite gneiss enclave displays similar concentrations of major elements and ASI (1.24), except for higher Fe_2O_3t (5.31 wt.%).

Rocks from the Chaidanuo granite have moderate to high rare earth element (REE) contents (ΣREE = 126–306). The chondrite-normalized REE patterns of all

Table 2
Whole-rock major and trace element analyses of the biotite monzogranites and biotite gneiss enclave in the NQOB.

Sample	Biotite monzogranite																	Enclave
	09QL-01	09QL-02	09QL-03	09Q-04	09QL-05	09QL-06	10QL-100	10QL-101	10QL-102	11QL-30	11QL-31	11QL-32	11QL-35	11QL-38	11QL-39	11QL-40	11QL-41	11QL-34
Majorelements(wt.%)																		
SiO_2	70.82	71.87	71.35	70.08	68.27	69.08	71.10	69.81	70.86	73.02	72.83	69.17	72.57	72.53	71.73	72.18	71.07	70.19
TiO_2	0.38	0.30	0.32	0.38	0.51	0.44	0.46	0.43	0.45	0.35	0.37	0.61	0.37	0.35	0.34	0.41	0.41	0.56
Al_2O_3	14.27	14.27	14.43	14.44	14.64	14.42	13.00	13.72	13.64	13.12	13.20	14.38	13.33	13.12	13.56	12.98	13.70	12.90
TFe_2O_3t	2.89	2.22	2.55	2.98	3.76	3.54	3.49	2.50	3.05	2.49	2.53	4.07	2.46	2.68	2.65	2.88	2.90	5.31
MnO	0.04	0.04	0.05	0.05	0.06	0.06	0.06	0.04	0.05	0.05	0.05	0.06	0.05	0.05	0.05	0.05	0.05	0.07
MgO	1.23	1.05	0.86	1.00	1.51	1.36	1.54	1.08	1.23	0.88	0.82	1.42	0.78	1.31	1.32	1.18	1.14	1.72
CaO	1.10	1.76	2.01	2.07	1.61	2.13	1.87	1.30	2.14	2.45	2.41	3.31	2.57	1.61	1.30	1.85	2.05	2.03
Na_2O	3.50	2.52	2.49	2.89	2.68	2.68	1.66	3.45	1.84	1.80	1.53	1.60	1.66	1.45	1.52	1.33	1.61	1.38
K_2O	4.52	4.62	4.67	4.63	4.93	4.83	4.77	5.58	4.89	4.00	4.10	3.37	4.23	4.57	5.44	5.16	5.31	4.12
P_2O_5	0.09	0.07	0.08	0.10	0.13	0.10	0.09	0.12	0.11	0.06	0.07	0.12	0.07	0.09	0.08	0.10	0.11	0.10
LOI	1.03	1.18	1.08	1.25	1.77	1.20	1.15	1.17	0.94	0.94	1.24	1.06	1.08	1.42	1.19	1.05	0.83	0.80
Total	99.88	99.91	99.89	99.88	99.85	99.84	99.19	99.21	99.19	99.16	99.16	99.17	99.16	99.18	99.19	99.18	99.19	99.18
ASI	1.13	1.16	1.13	1.07	1.16	1.07	1.15	0.97	1.12	1.12	1.16	1.17	1.11	1.28	1.26	1.17	1.13	1.24
K_2O/Na_2O	1.3	1.8	1.9	1.6	1.8	1.8	2.9	1.6	2.7	2.2	2.7	2.1	2.5	3.1	3.6	3.9	3.3	3.0
Mg#	0.38	0.40	0.32	0.32	0.36	0.36	0.39	0.38	0.37	0.34	0.32	0.33	0.31	0.41	0.42	0.37	0.36	0.32
Traceelements(ppm)																		
Li	10.3	20.1	37.1	9.40	16.8	44.7	30.8	8.58	22.5	9.07	8.43	9.10	10.30	32.7	33.7	24.6	21.6	27.6
P	393	305	305	480	524	436	406	457	453	282	344	527	307	412	369	426	451	413
Be	1.62	1.47	1.93	3.61	3.08	3.76												
Sc	9.33	6.48	6.81	8.47	10.2	10.1	7.85	6.68	6.95	6.27	7.60	10.3	6.72	7.36	7.20	6.90	6.81	11.4
Ti	2300	1740	1754	2436	3138	2836	3010	2626	2774	2195	2464	3930	2356	2452	2288	2730	2770	3404
V	37.6	17.1	20.1	31.4	42.0	38.0	36.0	24.8	30.5	27.0	32.0	50.6	28.4	27.2	26.2	30.2	30.5	60.9
Cr	10.8	6.53	10.4	14.0	23.1	25.2	22.0	18.6	23.3	13.2	5.93	11.7	7.80	19.4	17.0	15.0	14.5	11.5
Mn	322	300	368	343	406	446	345	218	296	292	335	389	289	317	330	290	292	431
Co	4.62	2.43	2.97	3.26	5.23	5.34	4.35	3.26	3.93	2.93	3.05	5.65	2.46	3.66	3.82	3.86	3.82	7.84
Ni	6.81	5.31	7.24	5.70	13.5	6.16	7.05	11.3	7.70	5.18	1.97	5.99	2.75	7.33	6.08	4.57	4.01	11.6
Cu	10.1	2.87	4.05	4.98	8.97	5.31	5.95	3.65	5.54	4.79	1.64	17.20	4.48	2.35	1.54	5.09	5.81	1.91
Zn	56.5	47.2	46.3	56.7	65.3	59.7	44.2	35.3	46.5	33.8	35.0	47.1	32.7	45.5	41.6	44.9	42.8	62.7
Ga	14.9	15.9	16.4	20.4	19.8	20.5	17.0	15.8	17.3	14.0	15.2	16.3	14.3	18.8	18.7	17.8	18.0	16.1
Rb	126	156	170	236	213	269	186	187	220	98.8	104	113	115	219	262	249	238	192
Sr	80.5	112	104	86.5	83.5	90.3	87.1	68.0	76.9	106	113	127	110	65.5	70.4	73.7	82.2	46.9
Y	37.7	36.8	36.8	59.0	37.2	46.5	37.0	30.0	34.4	35.3	40.8	36.7	33.6	36.6	35.0	35.3	35.7	68.6
Zr	166	154	149	221	266	168	225	233	218	147	153	233	175	197	195	287	245	139
Nb	14.4	11.3	12.1	32.6	22.3	19.4	31.5	36.2	38.4	18.0	21.4	22.9	18.9	32.2	31.9	37.4	37.2	36.6
Mo	0.24	0.37	0.15	0.40	0.52	0.15	1.86	1.07	2.97	2.03	1.04	2.89	1.48	1.93	1.05	2.53	1.46	1.32
Cs	1.27	2.16	2.86	3.12	4.03	7.85	4.46	1.00	6.83	1.05	0.90	2.37	0.78	6.20	8.05	7.30	7.00	11.6
Ba	602	532	468	369	533	445	516	460	429	550	563	697	523	436	974	457	506	333
La	27.4	28.8	28.7	60.5	57.9	36.9	40.3	38.9	45.6	24.8	27.4	40.2	27.9	37.7	37.4	51.1	46.4	23.8
Ce	57.9	58.3	58.4	129	133	80.4	88.4	83.5	100	48.4	54.1	80.9	54.5	84.3	83.1	114	105	51.3

Pr	6.65	6.56	6.61	15.55	15.0	9.46	10.22	9.72	11.8	5.50	6.15	9.03	6.23	9.70	9.55	13.0	11.8	6.32	
Nd	23.7	23.2	23.7	55.9	53.4	34.3	38.3	36.3	44.2	20.5	23.1	33.4	23.2	36.1	35.3	48.2	44.0	25.2	
Sm	4.94	4.60	4.82	11.00	9.80	7.23	7.69	7.23	8.74	4.39	5.04	6.56	4.79	7.45	7.29	9.25	8.63	6.40	
Eu	0.74	0.84	0.78	0.80	0.88	0.68	0.89	0.82	0.81	0.90	0.92	1.22	0.93	0.73	0.75	0.79	0.87	1.02	
Gd	5.05	4.84	4.92	9.93	8.33	7.12	7.09	6.40	7.56	4.87	5.54	6.53	4.98	6.66	6.43	7.84	7.42	7.62	
Tb	0.86	0.80	0.84	1.52	1.12	1.12	1.10	0.98	1.12	0.86	1.00	1.07	0.85	1.05	1.01	1.14	1.11	1.50	
Dy	5.63	5.36	5.38	8.96	6.26	6.88	6.78	5.76	6.52	5.91	6.74	6.82	5.65	6.43	6.17	6.55	6.51	10.94	
Ho	1.15	1.13	1.11	1.72	1.17	1.39	1.35	1.09	1.24	1.26	1.43	1.38	1.18	1.26	1.22	1.23	1.25	2.40	
Er	3.56	3.36	3.30	5.04	3.21	4.02	3.95	3.15	3.55	3.88	4.40	4.03	3.63	3.72	3.62	3.52	3.59	7.38	
Tm	0.53	0.51	0.49	0.70	0.43	0.59	0.56	0.44	0.50	0.58	0.65	0.57	0.54	0.54	0.53	0.50	0.50	1.09	
Yb	3.46	3.37	3.30	4.53	2.67	3.79	3.60	2.88	3.21	3.91	4.37	3.65	3.67	3.62	3.51	3.27	3.27	7.19	
Lu	0.48	0.47	0.47	0.63	0.37	0.53	0.51	0.41	0.45	0.56	0.62	0.52	0.53	0.52	0.50	0.47	0.47	1.01	
Hf	3.93	3.59	3.50	5.26	5.87	3.99	6.28	6.46	6.16	4.20	4.36	5.83	4.76	5.77	5.56	7.78	6.42	4.07	
Ta	0.90	0.57	0.80	2.22	1.21	1.36	2.58	2.55	2.71	1.15	1.34	3.17	1.74	2.80	2.82	2.96	2.51	1.92	
Pb	13.8	14.9	13.2	16.9	18.7	20.5	20.1	21.4	23.7	14.7	16.5	9.8	15.2	25.0	22.6	21.5	25.0	20.9	
Th	10.3	8.1	8.6	24.7	26.1	16.8	20.4	20.7	25.6	7.7	8.0	10.2	7.3	21.1	19.0	24.2	24.7	11.2	
U	2.73	1.34	1.52	3.92	2.26	3.44	3.90	3.59	3.53	1.64	1.99	2.31	1.90	5.08	3.84	3.61	3.68	3.05	
W							7.00	7.44	11.27	3.36	2.04	1.91	2.60	6.62	9.03	7.90	15.60	4.68	
Eu/Eu*	0.46	0.54	0.49	0.23	0.30	0.29	0.37	0.37	0.30	0.59	0.53	0.57	0.58	0.32	0.34	0.28	0.33	0.45	
REE	142	142	143	306	294	194	211	198	236	126	141	196	139	200	196	261	241	153	

LOI = loss on ignition; Fe_2O_3t = total iron; Mg# = Molecular $Mg^{2+}/(Mg + Fe^{2+})$; A/CNK = molecular $Al_2O_3/(CaO + Na_2O + K_2O)$; $Eu/Eu^* = Eu/\sqrt{Sm \times Gd}$.

samples from the pluton are characterized by LREE enrichments ($[La/Sm]_N = 3.3–4.1$), relatively flat HREE ($[Gd/Yb]_N = 1.0–2.6$) and a pronounced negative Eu anomaly ($Eu/Eu^* = 0.23–0.59$), while the enclave is relatively depleted in LREE and enriched in HREE with an evident Eu trough. Primitive-mantle normalized trace element diagrams invariably show a characteristic negative anomaly in Ba, Sr, Eu and HFSEs (Nb, Ta, Ti and P) and a positive anomaly in Th, U and Pb (Fig. 4).

4.2. Sr–Nd isotopic composition

Four biotite monzogranite samples from the Chaidanuo batholith show varied present-day $^{87}Sr/^{86}Sr$ ratios (0.7598–0.7780) but restricted $^{143}Nd/^{144}Nd$ ratios (0.5120–0.5121); the biotite gneiss enclave has the highest present-day $^{87}Sr/^{86}Sr$ (0.8400) and $^{143}Nd/^{144}Nd$ ratios (0.5122). The initial Sr isotope ratios, $I_{Sr}(t = 510\ Ma)$, of the granite samples range from 0.7310 to 0.7436, lower than that of the biotite gneiss enclave ($I_{Sr}(t = 510\ Ma) = 0.7539$). The $\varepsilon_{Nd}(t)$ values and two-stage Nd model ages (T_{DM2}) are essentially the same for both the host granite (−6.0 to −7.1 and 1718–1808 Ma) and the biotite gneiss enclave (−5.6 and 1638 Ma) (Table 3).

4.3. Zircon U–Pb ages

Zircon U–Pb age dating was done for three samples (09QL-01, 09QL-03 and 11QL-35) from the host granite, two samples (11QL-34 and 12QL-61) from the biotite gneiss and mafic magmatic enclaves, and one sample (12QL-64) from the granitic country rocks (see Fig. 1 for localities).

4.3.1. Granite pluton

Zircons from the host pluton are euhedral, elongated crystals 50–150 μm in length. CL images and U–Pb analyses reveal that these zircons commonly have core-rim structures and can be subdivided into two groups: an inherited group and a magmatic group.

Zircons with inherited cores exhibit complex inner structures with irregular shapes, high luminescent, structure-less or weak oscillatory bands mantled by a relatively dark and narrow oscillatory zoned rim, or simply as unmantled, subrounded or rarely euhedral grains with homogeneous magmatic oscillatory zones (Fig. 5a and b). In sample 09QL-01, one bright and homogenous luminescent core yields a $^{206}Pb/^{238}U$ age of 954 ± 11 Ma with a Th/U ratio of 0.52, interpreted as magmatic origin; another one gives $^{206}Pb/^{238}U$ age of 837 ± 9 Ma. The date of 637 ± 7 Ma plots somewhat away from the concordant curve, suggesting incomplete radiogenic lead loss due to later magmatic events. Thirteen analyses, fluctuating between 747 and 767 Ma, form a coherent group, giving a weighted mean $^{206}Pb/^{238}U$ age of 751 ± 6 Ma with Th/U ratios > 0.1 (MSWD = 1.2) (Fig. 6a). In sample 09QL-03, three datapoints give a weighted mean $^{206}Pb/^{238}U$ age of 741 ± 9 Ma (MSWD = 0.81) (Fig. 6b). Except for the 603 Ma data-point, the dates of 557, 664, 705 and 795 Ma are geologically insignificant as they represent mixing ages

Table 3
Sr–Nd isotopic composition for the biotite monzogranites and biotite gneiss enclave.

Sample	$^{87}Rb/^{86}Sr$	$^{87}Sr/^{86}Sr$	2σ	$I_{Sr}(t)$	$^{147}Sm/^{144}Nd$	$^{143}Nd/^{144}Nd$	2σ	t(Ma)	$\varepsilon_{Nd}(0)$	$\varepsilon_{Nd}(t)$	$f_{Sm/Nd}$	T_{DM2} (Ma)
Biotite monzogranites												
09QL-01	4.549	0.7640	4	0.7310	0.126	0.5121	8	510	−10.8	−6.2	−0.36	1850
09QL-03	4.747	0.7780	4	0.7436	0.123	0.5120	7	510	−11.9	−7.1	−0.37	1882
11QL-32	2.592	0.7541	4	0.7353	0.119	0.5121	5	510	−11.0	−6.0	−0.40	1728
11QL-35	3.048	0.7598	4	0.7377	0.125	0.5121	2	510	−11.0	−6.3	−0.36	1843
The biotite gneiss enclave												
11QL-34	11.86	0.8400	4	0.7539	0.153	0.5122	4	510	−8.4	−5.6	−0.22	2370

Note: $f_{Sm/Nd} = (^{147}Sm/^{144}Nd)_S/(^{147}Sm/^{144}Nd)_{CHUR(0)} - 1$; $\varepsilon_{Nd}(0) = ((^{143}Nd/^{144}Nd)_S/(^{143}Nd/^{144}Nd)_{CHUR(0)} - 1) \times 10{,}000$; $\varepsilon_{Nd}(t) = \{[(^{143}Nd/^{144}Nd)_S - (^{147}Sm/^{144}Nd)_S \times (e^{\lambda t} - 1)]/[(^{143}Nd/^{144}Nd)_{CHUR(0)} - (^{147}Sm/^{144}Nd)_{CHUR(0)} \times (e^{\lambda t} - 1) - 1]\} \times 10{,}000$; $T_{DM1} = 1000/\lambda \times \ln\{1 + [(^{143}Nd/^{144}Nd)_S - (^{143}Nd/^{144}Nd)_{DM}]/[(^{147}Sm/^{144}Nd)_S - (^{147}Sm/^{144}Nd)_{DM}]\}$; $T_{DM2} = T_{DM1} - (T_{DM1} - t) \times (f_{CC} - f_S)/(f_{CC} - f_{DM})$ (Li et al., 2003), where $\varepsilon_{Nd}(t)$ values were calculated using $(^{147}Sm/^{144}Nd)_{CHUR(0)} = 0.1967$ and $(^{143}Nd/^{144}Nd)_{CHUR(0)} = 0.512638$, and T_{DM} values were calculated using present-day $(^{143}Nd/^{144}Nd)_{DM} = 0.51315$ and $(^{147}Sm/^{144}Nd)_{DM} = 0.2137$. $I_{Sr}(t) = (^{87}Sr/^{86}Sr)_S - (^{87}Rb/^{86}Sr)_S \times (e^{\lambda t} - 1)$ $\lambda_{Sm-Nd} = 6.535 \times 10^{-12}$ year^{-1}; $\lambda_{Rb-Sr} = 1.42 \times 10^{-11}$ year^{-1}. $t = 510$ Ma.

of two different zircon domains as indicated by CL images. Two old $^{207}Pb/^{206}Pb$ ages of 1683 ± 46 and 1440 ± 21 Ma were obtained in samples 09QL-03 and 11QL-35. Five analyses in sample 11QL-35 scatter in a wide $^{206}Pb/^{238}U$ range of 591–762 Ma with Th/U ratios of 0.07–0.83 (Fig. 6c). In summary, inherited cores of zircons are abundant in the host granite and they yield a dominant, magmatic age group of ~750 Ma with minor magmatic/metamorphic ages of 591–1683 Ma.

Zircons from the magmatic group (also termed '~510 Ma group') show perfect oscillatory-zoned structures of magmatic origin (Fig. 5a and b). Seven concordant datapoints in sample 09QL-01 yield $^{206}Pb/^{238}U$ ages of 510–520 Ma with varying Th/U ratios of 0.14–0.86 and define a weighted mean age of 516 ± 4 Ma (MSWD = 0.31) (Fig. 6a). Thirteen analyses in sample 09QL-03 gives a concordant weighted $^{206}Pb/^{238}U$ mean age of 510 ± 4 Ma (MSWD = 1.3) with variable Th/U ratios of 0.05–0.64 (most >0.1) (Fig. 6b). In sample 11QL-35, the magmatic zircon rims exhibit huge variation of Th and U concentrations (Th 73–3638 ppm, U 160–3749 ppm) with Th/U ratios of 0.28–1.16. Fourteen analyses give a weighted mean $^{206}Pb/^{238}U$ age of 505 ± 8 Ma (MSWD = 3.1) (Fig. 6c). Thus, ages of ~516–505 Ma are interpreted to be crystallization ages of the Chaidanuo granitic batholith.

4.3.2. The biotite gneiss enclave

Zircons separated from the biotite gneiss enclave sample (11QL-34) are subhedral, short-prismatic crystals and ~50–150 μm long with length/width ratios of ~2:1. They show evident core-rim structures in CL images; the corroded cores are moderately luminescent with blurry magmatic oscillatory zones, surrounded by dull luminescent rims with or without weak oscillatory zoning (Fig. 5c). Most core domains are molted into irregular or embayed shapes, which indicate an overprinting by subsequent metamorphic/anatectic events.

Twenty-five zircons were analyzed using the SIMS method. The cores have relatively uniform U (251–736 ppm) and Th (73–191 ppm) and Th/U ratios (0.18–0.36). Except for the two inner cores that give old $^{207}Pb/^{206}Pb$ ages of 1225 ± 26 and 1632 ± 19 Ma, 13 analyses form a coherent population with a weighted mean $^{206}Pb/^{238}U$ age of 744 ± 10 Ma (MSWD = 2.2), representing the primary magmatic age of the biotite gneiss enclave. The dark luminescent rims show huge U (497–4939 ppm) variation, low Th (34–298 ppm) and Th/U ratios (0.01–0.08), suggesting metamorphic/anatectic origin (e.g., Song et al., 2010a). Ten spots give a weighted mean $^{206}Pb/^{238}U$ age of 503 ± 5 Ma (MSWD = 1.2) (Fig. 6d). The remaining date of 551 Ma is likely a mixing age based on its CL image.

4.3.3. Mafic magmatic enclave

Zircons from the mafic-magmatic-enclave sample (12QL-61) are euhedral and show a weakly oscillatory-zoned structure of magmatic origin (Fig. 5d). The U content in these zircons ranges from 617 to 1933 ppm and Th from 87 to 311 ppm with Th/U ratios of 0.10–0.35 (Table 4). Twenty-eight analyses yield $^{206}Pb/^{238}U$ ages ranging from 502 to 518 Ma with a weighted mean age of 510 ± 2 Ma (MSWD = 1.04) (Fig. 6e), representing the crystallization age of the mafic magmatic enclave.

4.3.4. Wall-rock granitic gneiss

Zircons from the granitic gneiss sample (12QL-64) in the country-rock are euhedral and transparent crystals 50–100 μm in length. They are characterized by large homogeneous cores with oscillatory-zoning surrounded by dark, thin metamorphic rims (<1 μm in width) (Fig. 5e). The magmatic cores have relatively low Th (36–166 ppm) and U (74–300 ppm) contents with Th/U ratios of 0.14–0.63, similar to those in the 744 Ma magmatic cores of the biotite gneiss enclave (Table 4). Twenty-five spots made on the igneous cores by the LA-ICP-MS method give a weighted mean $^{206}Pb/^{238}U$ age of 746 ± 3 Ma (MSWD = 0.54), representing the crystallization age of the granitic country rock (Fig. 6f).

4.4. Zircon Hf isotopic composition

Zircon grains from samples 09QL-01 and 09QL-03 with ages of ~516–510 Ma exhibit variable initial $^{176}Hf/^{177}Hf$ ratios, from 0.282047 to 0.282320, with $\varepsilon_{Hf}(t)$ values from -14.8 ± 0.7 to -4.7 ± 0.5 and two-stage model ages

Table 4
LA-ICP-MS zircon U–Pb data for the biotite monzogranites, wall-rock granitic gneiss and mafic magmatic enclave.

Sample	Type*	^{232}Th	^{238}U	Th/U	Ti	T	Ratios						Ages (Ma)						Disc. (%)
							^{207}Pb/^{206}Pb	1σ	^{207}Pb/^{235}U	1σ	^{206}Pb/^{238}U	1σ	^{207}Pb/^{206}Pb	1σ	^{207}Pb/^{235}U	1σ	^{206}Pb/^{238}U	1σ	
Biotite monzogranite (09QL-01)																			
1	I1	151	289	0.52	6.96	722	0.06526	0.00131	1.12954	0.02288	0.12553	0.00145	783	24	768	11	762	8	1
2	I2	72	398	0.18	5.65	704	0.0653	0.00151	0.93528	0.02166	0.10387	0.00124	784	29	670	11	637	7	5
3	I1	64	224	0.28	14.9	796	0.06447	0.00133	1.1201	0.02322	0.12601	0.00148	757	25	763	11	765	8	0
4	Mag	160	459	0.35	3.53	665	0.0579	0.00139	0.66534	0.01597	0.08334	0.001	526	32	518	10	516	6	0
5	Mag	221	884	0.25	7.66	731	0.0571	0.00184	0.65769	0.01977	0.08353	0.00098	496	73	513	12	517	6	−1
6	I1	58	230	0.25	12.6	779	0.06416	0.00133	1.08513	0.02269	0.12267	0.00144	747	25	746	11	746	8	0
7	Mag	264	307	0.86	7.05	723	0.05744	0.00128	0.65815	0.01472	0.0831	0.00098	508	29	513	9	515	6	0
8	Mag	79	225	0.35	51.6	941	0.05676	0.00226	0.64464	0.02428	0.08237	0.00105	482	90	505	15	510	6	−1
9	Mag	244	983	0.25	11.3	768	0.05798	0.0018	0.67282	0.0194	0.08416	0.00098	529	70	522	12	521	6	0
10	I1	55	373	0.15	7.34	727	0.06324	0.0017	1.05695	0.02563	0.12122	0.0014	716	58	732	13	738	8	−1
11	I2	342	652	0.52	26.3	858	0.07589	0.00238	1.66848	0.0484	0.15946	0.00191	1092	64	997	18	954	11	5
12	I1	74	112	0.66	31.6	879	0.06437	0.00188	1.08445	0.03164	0.12219	0.00152	754	41	746	15	743	9	0
13	I1	58	207	0.28	12.1	775	0.06402	0.00137	1.11487	0.02403	0.1263	0.00148	742	26	761	12	767	8	−1
14	Mag	55	386	0.14	65.8	975	0.05843	0.00152	0.67392	0.01745	0.08365	0.00102	546	35	523	11	518	6	1
15	I1	185	429	0.43	8.25	738	0.06922	0.00134	1.18358	0.02321	0.124	0.00143	905	22	793	11	754	8	5
16	I1	62	251	0.25	14.6	793	0.06506	0.00143	1.11537	0.02474	0.12433	0.00145	776	27	761	12	755	8	1
17	Mag	147	551	0.27	5.72	705	0.05756	0.00139	0.65978	0.01594	0.08313	0.001	513	32	514	10	515	6	0
18	I2	55	284	0.19	7.02	723	0.06707	0.00154	1.28144	0.0295	0.13857	0.00167	840	28	837	13	837	9	0
19	I1	86	447	0.19	6.95	722	0.06654	0.00175	1.12232	0.02938	0.12232	0.00152	823	34	764	14	744	9	3
20	I1	40	219	0.18	10.2	757	0.06482	0.00192	1.09397	0.02967	0.1224	0.00147	769	64	750	14	744	8	1
21	I1	50	359	0.14	6.85	721	0.06425	0.00131	1.0906	0.02261	0.12311	0.00144	750	25	749	11	748	8	0
22	I1	66	262	0.25	9.52	751	0.06374	0.00156	1.08304	0.02659	0.12322	0.00148	733	32	745	13	749	8	−1
23	I1	147	318	0.46	6.15	711	0.06426	0.00143	1.08798	0.02446	0.12278	0.00146	750	28	748	12	747	8	0
Biotite monzogranite (09QL-03)																			
1	I2	31	375	0.08	5.24	697	0.05948	0.00124	0.80447	0.01704	0.09808	0.00115	585	26	599	10	603	7	−1
2	I1	66	195	0.34	43.4	919	0.06315	0.00233	1.00634	0.03498	0.11558	0.00144	713	80	707	18	705	8	0
3	Mag	29	155	0.19	3.84	672	0.05743	0.00164	0.64917	0.01853	0.08198	0.00103	508	41	508	11	508	6	0
4	Mag	2	39	0.05	87.8	1017	0.05767	0.00295	0.65755	0.03322	0.08268	0.00126	517	84	513	20	512	8	0
5	Mix	60	169	0.36	38.6	904	0.06167	0.00171	0.92198	0.02557	0.10841	0.00134	663	38	663	14	664	8	0
6	Mag	166	280	0.59	17.1	810	0.05772	0.00288	0.63608	0.03064	0.07993	0.00103	519	112	500	19	496	6	1
7	Mag	318	1040	0.31	4.55	686	0.05766	0.00182	0.65512	0.01919	0.0824	0.00098	517	71	512	12	510	6	0
8	Mag	41	634	0.07	10.8	763	0.05932	0.00122	0.68157	0.01423	0.08333	0.00097	579	26	528	9	516	6	2
9	Mag	72	604	0.12	7.25	726	0.05867	0.00138	0.66134	0.01563	0.08174	0.00098	555	31	515	10	507	6	2
10	I2	62	294	0.21	7.39	728	0.10321	0.00249	4.03981	0.08533	0.28388	0.00329	1683	46	1642	17	1611	17	4
11	Mag	54	152	0.36	19.2	823	0.0574	0.00203	0.64403	0.02279	0.08137	0.00102	507	56	505	14	504	6	0
12	Mix	68	170	0.40	14.9	795	0.05899	0.00149	0.73341	0.0186	0.09017	0.0011	567	34	559	11	557	7	0
13	I1	71	223	0.32	10.3	759	0.06489	0.00198	1.10207	0.031	0.12318	0.00148	771	66	754	15	749	8	1
14	Mag	268	417	0.64	28.3	866	0.06013	0.00134	0.68639	0.01548	0.08278	0.00098	608	29	531	9	513	6	4
15	Mag	82	324	0.25	16.0	803	0.06053	0.00142	0.69309	0.01644	0.08304	0.00099	623	31	535	10	514	6	4

(*continued on next page*)

Table 4 (*continued*)

Sample	Type*	^{232}Th	^{238}U	Th/U	Ti	T	Ratios						Ages (Ma)						Disc. (%)
							^{207}Pb/^{206}Pb	1σ	^{207}Pb/^{235}U	1σ	^{206}Pb/^{238}U	1σ	^{207}Pb/^{206}Pb	1σ	^{207}Pb/^{235}U	1σ	^{206}Pb/^{238}U	1σ	
16	Mag	24	170	0.14	9.35	749	0.05701	0.00173	0.64515	0.01953	0.08206	0.00102	492	45	505	12	508	6	−1
17	Mag	177	511	0.35	8.37	739	0.05876	0.00134	0.66063	0.01521	0.08153	0.00097	558	30	515	9	505	6	2
18	Mix	66	228	0.29	13.7	787	0.06549	0.00185	1.18577	0.0335	0.1313	0.00168	790	38	794	16	795	10	0
19	I1	111	456	0.24	10.6	762	0.06449	0.00182	1.07338	0.02748	0.12072	0.00143	758	61	740	13	735	8	1
20	I1	72	323	0.22	14.0	789	0.06486	0.00186	1.08697	0.02837	0.12154	0.00144	770	62	747	14	739	8	1
21	Mag	39	90	0.43	14.6	793	0.05745	0.00205	0.65135	0.02303	0.08221	0.0011	509	54	509	14	509	7	0
22	Mag	99	222	0.45	7.22	726	0.05806	0.00147	0.67984	0.01733	0.08491	0.00104	532	35	527	10	525	6	0
Wall-rock granitic gneiss (12QL-64)																			
1	Mag	63	223	0.28	9.62	742	0.06586	0.00138	1.10251	0.02265	0.12148	0.00141	802	43	755	11	739	8	2
2	Mag	52	201	0.26	12.5	767	0.06474	0.00136	1.10626	0.02280	0.12400	0.00143	766	44	756	11	754	8	0
3	Mag	80	183	0.44	5.03	685	0.06442	0.00142	1.10053	0.02377	0.12398	0.00145	755	46	754	11	753	8	0
4	Mag	94	201	0.47	6.49	707	0.06627	0.00148	1.12801	0.02469	0.12351	0.00145	815	46	767	12	751	8	2
5	Mag	63	207	0.31	11.0	755	0.06504	0.00138	1.09841	0.02289	0.12254	0.00142	776	44	753	11	745	8	1
6	Mag	166	300	0.55	4.01	667	0.06446	0.00131	1.08139	0.02159	0.12173	0.00139	757	42	744	11	741	8	1
7	Mag	54	288	0.19	9.72	743	0.06539	0.00136	1.10254	0.02263	0.12236	0.00141	787	43	755	11	744	8	1
8	Mag	104	225	0.46	5.60	694	0.06476	0.00136	1.09202	0.02264	0.12236	0.00142	767	44	750	11	744	8	1
9	Mag	47	202	0.23	8.65	732	0.06412	0.00138	1.08509	0.02296	0.12281	0.00143	746	45	746	11	747	8	0
10	Mag	50	109	0.46	16.5	795	0.06505	0.00170	1.09910	0.02818	0.12260	0.00156	776	54	753	14	746	9	1
11	Mag	36	118	0.31	18.6	807	0.06449	0.00156	1.10449	0.02626	0.12427	0.00152	758	50	756	13	755	9	0
12	Mag	38	168	0.23	7.24	716	0.06403	0.00145	1.08539	0.02411	0.12301	0.00146	743	47	746	12	748	8	0
13	Mag	48	190	0.25	8.29	729	0.06654	0.00148	1.13204	0.02469	0.12346	0.00146	823	46	769	12	750	8	2
14	Mag	105	219	0.48	4.87	683	0.06511	0.00138	1.11362	0.02328	0.12411	0.00144	778	44	760	11	754	8	1
15	Mag	85	190	0.45	6.32	705	0.06626	0.00143	1.12386	0.02386	0.12308	0.00144	815	44	765	11	748	8	2
16	Mag	116	207	0.56	5.18	688	0.06786	0.00144	1.13892	0.02385	0.12179	0.00141	864	43	772	11	741	8	4
17	Mag	47	74	0.63	21.7	824	0.06285	0.00186	1.05730	0.03075	0.12208	0.00161	703	62	733	15	743	9	−1
18	Mag	61	231	0.27	10.6	752	0.06451	0.00158	1.09281	0.02644	0.12293	0.00142	758	51	750	13	747	8	0
19	Mag	69	221	0.31	12.6	768	0.06514	0.00141	1.07967	0.02306	0.12028	0.00141	779	45	744	11	732	8	2
20	Mag	146	270	0.54	5.36	691	0.06475	0.00138	1.08771	0.02282	0.12189	0.00141	766	44	747	11	742	8	1
21	Mag	43	295	0.14	5.73	696	0.06594	0.00135	1.10384	0.02226	0.12148	0.00139	804	42	755	11	739	8	2
22	Mag	62	157	0.39	5.80	697	0.06529	0.00150	1.10926	0.02507	0.12327	0.00147	784	47	758	12	749	8	1
23	Mag	41	250	0.17	8.49	731	0.06489	0.00137	1.11285	0.02327	0.12444	0.00144	771	44	760	11	756	8	0
24	Mag	52	208	0.25	10.1	747	0.06397	0.00141	1.08417	0.02356	0.12297	0.00144	741	46	746	11	748	8	0
25	Mag	47	164	0.29	9.28	739	0.06493	0.00152	1.08571	0.02510	0.12133	0.00146	772	49	746	12	738	8	1
Mafic magmatic enclave (12QL-61)																			
1	Mag	115	1061	0.11	4.68	679	0.05784	0.00081	0.64685	0.00910	0.08113	0.00088	523	31	507	6	503	5	1
2	Mag	87	831	0.10	4.41	674	0.05733	0.00083	0.64499	0.00942	0.08161	0.00089	504	32	505	6	506	5	0
3	Mag	135	868	0.16	12.1	764	0.05762	0.00085	0.64603	0.00953	0.08134	0.00089	515	32	506	6	504	5	0
4	Mag	242	690	0.35	19.9	815	0.05885	0.00116	0.67061	0.01302	0.08266	0.00096	562	42	521	8	512	6	2
5	Mag	149	1080	0.14	4.98	684	0.05830	0.00080	0.67164	0.00932	0.08357	0.00090	541	31	522	6	517	5	1
6	Mag	174	786	0.22	8.89	735	0.05789	0.00082	0.64731	0.00924	0.08112	0.00088	525	31	507	6	503	5	1

7	Mag	150	934	0.16	7.84	724	0.05768	0.00079	0.64577	0.00892	0.08122	0.00088	517	30	506	6	503	5	0
8	Mag	86	813	0.11	6.72	710	0.05753	0.00083	0.65759	0.00953	0.08292	0.00090	512	32	513	6	514	5	0
9	Mag	136	1203	0.11	6.82	711	0.05715	0.00077	0.63832	0.00865	0.08103	0.00087	497	30	501	5	502	5	0
10	Mag	141	1039	0.14	5.42	691	0.05756	0.00081	0.64762	0.00914	0.08163	0.00088	513	31	507	6	506	5	0
11	Mag	131	752	0.17	6.04	701	0.05735	0.00083	0.65319	0.00952	0.08262	0.00090	505	32	510	6	512	5	0
12	Mag	154	1189	0.13	5.74	696	0.05717	0.00077	0.65793	0.00894	0.08349	0.00090	497	30	513	5	517	5	−1
13	Mag	128	1279	0.10	4.93	684	0.05803	0.00076	0.66301	0.00876	0.08288	0.00089	531	29	517	5	513	5	1
14	Mag	110	1080	0.10	4.20	670	0.05796	0.00079	0.65691	0.00905	0.08222	0.00089	528	30	513	6	509	5	1
15	Mag	149	1037	0.14	8.49	731	0.05818	0.00079	0.66424	0.00907	0.08282	0.00089	536	30	517	6	513	5	1
16	Mag	121	727	0.17	7.88	724	0.05743	0.00085	0.65100	0.00961	0.08223	0.00090	508	32	509	6	509	5	0
17	Mag	122	847	0.14	7.66	721	0.05842	0.00082	0.67009	0.00948	0.08321	0.00090	545	31	521	6	515	5	1
18	Mag	150	690	0.22	6.41	706	0.05664	0.00085	0.63464	0.00950	0.08128	0.00089	477	33	499	6	504	5	−1
19	Mag	123	674	0.18	7.45	719	0.05850	0.00087	0.67532	0.01006	0.08374	0.00092	549	32	524	6	518	5	1
20	Mag	133	1281	0.10	4.17	670	0.05748	0.00076	0.65302	0.00871	0.08241	0.00088	510	29	510	5	511	5	0
21	Mag	188	617	0.30	9.43	740	0.05895	0.00087	0.66033	0.00980	0.08126	0.00089	565	32	515	6	504	5	2
22	Mag	114	928	0.12	5.54	693	0.05818	0.00080	0.65510	0.00908	0.08168	0.00088	536	30	512	6	506	5	1
23	Mag	187	1628	0.11	4.69	679	0.05814	0.00074	0.67007	0.00865	0.08361	0.00089	534	28	521	5	518	5	1
24	Mag	145	799	0.18	10.4	750	0.05778	0.00088	0.65487	0.00993	0.08221	0.00090	521	33	512	6	509	5	0
25	Mag	194	1166	0.17	8.41	730	0.05712	0.00078	0.64388	0.00882	0.08178	0.00088	496	30	505	5	507	5	0
26	Mag	311	1933	0.16	6.75	710	0.05745	0.00075	0.66200	0.00874	0.08359	0.00089	509	28	516	5	518	5	0
27	Mag	222	1820	0.12	3.96	666	0.05729	0.00073	0.65912	0.00852	0.08346	0.00089	502	28	514	5	517	5	−1
28	Mag	186	1678	0.11	9.76	744	0.05774	0.00076	0.66063	0.00874	0.08300	0.00089	520	29	515	5	514	5	0

Dis. (%) describes degree of discordance; common Pb was corrected using the method by Andersen (2002).

* (1) Inherited zircons: I1 and I2; (2) magmatic zircons: Mag; (3) mixed ages: Mix; (4) metamorphic ages: Meta.

Table 5
SIMS zircon U–Pb data for the host biotite monzogranite and biotite gneiss enclave.

Sample	Type*	^{232}Th	^{238}U	Th/U	f_{206}%	Ratios						Ages (Ma)					
						^{207}Pb/^{206}Pb	1σ	^{207}Pb/^{235}U	1σ	^{206}Pb/^{238}U	1σ	^{207}Pb/^{206}Pb	1σ	^{207}Pb/^{235}U	1σ	^{206}Pb/^{238}U	1σ
The biotite gneiss enclave (11QL-34)																	
1	I1	74	405	0.183	{0.31}	0.06021	2.49	1.01917	2.91	0.1228	1.5	611	53	714	15	747	11
2	I1	155	452	0.344	{0.27}	0.06093	2.24	1.0318	2.69	0.1228	1.5	637	47	720	14	747	11
3	Meta	34	497	0.068	{0.08}	0.05746	2.08	0.63587	2.56	0.0803	1.5	509	45	500	10	498	7
4	I2	379	597	0.636	{0.05}	0.1004	1.04	3.27809	1.83	0.2368	1.5	1632	19	1476	14	1370	19
5	I1	122	423	0.288	{0.09}	0.06322	1.75	1.04952	2.31	0.1204	1.5	716	37	729	12	733	10
6	Meta	68	3187	0.021	{0.22}	0.05713	0.92	0.64982	1.76	0.0825	1.5	497	20	508	7	511	7
7	I1	173	560	0.309	{0.25}	0.0643	1.82	1.07885	2.36	0.1217	1.5	752	38	743	13	740	11
8	I1	191	536	0.357	{0.16}	0.06276	1.57	1.0892	2.17	0.1259	1.5	700	33	748	12	764	11
9	I1	135	427	0.315	{0.14}	0.06466	1.77	1.06706	2.32	0.1197	1.5	763	37	737	12	729	10
10	I2	416	472	0.882	{0.09}	0.08117	1.31	2.11396	2	0.1889	1.5	1226	26	1153	14	1115	15
11	I1	73	251	0.292	{0.27}	0.06232	2.78	1.04059	3.16	0.1211	1.5	685	58	724	17	737	11
12	I1	162	476	0.341	{0.54}	0.06369	2.11	1.08256	2.59	0.1233	1.5	731	44	745	14	749	11
13	Mix	48	534	0.09	{0.05}	0.05831	1.91	0.71732	2.43	0.0892	1.5	541	41	549	10	551	8
14	Meta	79	1444	0.055	{0.07}	0.05764	1.23	0.64114	1.94	0.0807	1.5	516	27	503	8	500	7
15	I1	124	465	0.266	{0.19}	0.06023	1.97	0.97581	2.48	0.1175	1.51	612	42	692	13	716	10
16	I1	110	378	0.292	{0.17}	0.06418	1.85	1.09962	2.38	0.1243	1.5	748	39	753	13	755	11
17	I1	157	439	0.357	{0.13}	0.06526	1.71	1.10509	2.27	0.1228	1.5	783	35	756	12	747	11
18	I1	78	295	0.265	{0.18}	0.06655	2.01	1.10393	2.51	0.1203	1.5	824	41	755	14	732	10
19	Meta	88	4939	0.018	{0.04}	0.05748	0.59	0.65255	1.62	0.0823	1.5	510	13	510	7	510	7
20	I1	85	330	0.256	{0.14}	0.06253	1.98	1.10648	2.5	0.1283	1.53	692	42	757	13	778	11
21	Meta	43	4198	0.01	{0.04}	0.05745	0.79	0.65836	1.69	0.0831	1.5	509	17	514	7	515	7
22	Meta	106	2136	0.05	{0.42}	0.05828	1.17	0.6364	1.9	0.0792	1.5	540	25	500	8	491	7
23	Meta	62	1871	0.033	{0.65}	0.05818	1.37	0.65781	2.03	0.082	1.5	537	30	513	8	508	7
24	Meta	298	3884	0.077	{0.41}	0.05647	0.93	0.6282	1.77	0.0807	1.5	471	20	495	7	500	7
25	Meta	60	1776	0.034	{0.04}	0.05715	1	0.64341	1.8	0.0817	1.5	497	22	504	7	506	7
26	Meta	56	1731	0.032	{0.07}	0.0568	1.05	0.62276	1.83	0.0795	1.5	484	23	492	7	493	7
Biotite monzogranite (11QL-35)																	
1	Mag	1049	1991	0.527	{3.08}	0.05837	2.77	0.65155	3.15	0.081	1.5	544	60	509	13	502	7
2	Mag	450	1212	0.371	{0.15}	0.05748	2.05	0.64246	2.9	0.0811	2.05	510	45	504	12	502	10
3	Mag	2144	3530	0.607	{0.45}	0.05681	0.96	0.64801	1.78	0.0827	1.5	484	21	507	7	512	7
4	Mag	202	730	0.277	{0.58}	0.05741	2.82	0.61059	3.19	0.0771	1.5	507	61	484	12	479	7
5	Mag	299	592	0.504	{0.15}	0.05826	1.98	0.67427	2.48	0.0839	1.5	540	43	523	10	520	8
6	Mag	148	316	0.47	{0.10}	0.05852	2.46	0.67292	2.89	0.0834	1.52	549	53	523	12	516	8
7	Mag	74	160	0.46	{1.02}	0.05459	6.83	0.58336	6.99	0.0775	1.51	395	146	467	27	481	7
8	Mag	291	825	0.353	{0.13}	0.05729	1.61	0.66317	2.21	0.084	1.52	503	35	517	9	520	8
9	Mag	240	625	0.384	{0.17}	0.0563	1.9	0.63765	2.55	0.0822	1.7	464	42	501	10	509	8
10	I2	305	954	0.32	{0.07}	0.05997	1.2	0.79356	1.92	0.096	1.5	603	26	593	9	591	9
11	Mag	529	1893	0.279	{0.03}	0.05779	1.24	0.67141	1.95	0.0843	1.5	522	27	522	8	522	8
12	Mag	425	1433	0.296	{0.07}	0.05746	1.19	0.64566	1.91	0.0815	1.5	509	26	506	8	505	7
13	I2	248	460	0.539	{0.13}	0.0907	1.13	2.90795	1.88	0.2325	1.5	1440	21	1384	14	1348	18
14	I2	134	825	0.163	{0.10}	0.06122	1.51	0.90062	2.13	0.1067	1.5	647	32	652	10	654	9
15	Mag	73	174	0.423	{0.67}	0.05258	8.26	0.59135	8.39	0.0816	1.51	311	178	472	32	506	7
16	Mag	3638	3749	0.97	{0.48}	0.05615	1.22	0.62807	1.94	0.0811	1.5	458	27	495	8	503	7
17	I1	547	659	0.83	{0.13}	0.06277	2.33	1.05152	2.8	0.1215	1.55	701	49	730	15	739	11
18	I1	72	383	0.188	{0.17}	0.06367	1.86	1.10119	2.39	0.1254	1.5	731	39	754	13	762	11
19	I2	362	1045	0.346	{0.57}	0.06121	1.83	0.84317	2.37	0.0999	1.5	647	39	621	11	614	9
20	Mag	954	823	1.16	{1.56}	0.05733	2.9	0.64445	3.26	0.0815	1.5	504	63	505	13	505	7

* (1) Inherited zircons: I1 and I2; (2) magmatic zircons: Mag; (3) mixed ages: Mix.

(T_{DM2}) between 1776 and 2395 Ma (Table 6; Fig. 7). The 750 Ma zircons also display a wide range of initial ^{176}Hf/^{177}Hf ratios, from 0.282070 to 0.282432, $\varepsilon_{Hf}(t)$ from -8.4 ± 0.7 to 4.8 ± 0.7, and T_{DM2} values, 1366 to 2184 Ma, respectively. The 795 Ma zircon core of mixed origin in sample 09QL-03 yield extremely low initial ^{176}Hf/^{177}Hf ratio (0.281641), $\varepsilon_{Hf}(t)$ value (-22.5 ± 0.7) and old model age of 3101 Ma (Table 6; Fig. 7). Three older zircon cores with ^{206}Pb/^{238}U ages of 837–954 Ma have ^{176}Hf/^{177}Hf ratios of 0.281985–0.282240, $\varepsilon_{Hf}(t)$ values of -6.8 to $+1.5$ and T_{DM2} of 1693–2241 Ma. Zircon from the mafic magmatic enclave (12QL-61) has variable, but more depleted Hf isotopic composition with initial ^{176}Hf/^{177}Hf ratios of 0.282284–0.282514, $\varepsilon_{Hf}(t)$ values of -6.0 to $+2.1$ than the 510-Ma zircons from the host granite (Table 6; Fig. 7). The calculated single-stage model ages are

Table 6
Zircon Lu–Hf isotopic data for the host biotite monzogranites and mafic magmatic enclave.

Sample	$^{176}Yb/^{177}Hf$	$^{176}Lu/^{177}Hf$	$^{176}Hf/^{177}Hf$	$\pm(2\sigma)$	$^{206}Pb/^{238}U$ Age (Ma)	$(^{176}Hf/^{177}Hf)_i$	$\varepsilon_{Hf}(t)$	$\pm(2\sigma)$	T_{DM1} (Ma)	$\pm(2\sigma)$	T_{DM2} (Ma)	$\pm(2\sigma)$	$f_{Lu/Hf}$
09QL-01 01	0.098469	0.003571	0.282302	0.000024	921	0.282240	1.5	0.8	1440	72	1693	107	−0.89
09QL-01 02	0.025268	0.000889	0.282445	0.000019	762	0.282432	4.8	0.7	1139	53	1366	84	−0.97
09QL-01 03	0.037425	0.001208	0.282211	0.000017	765	0.282193	−3.6	0.6	1478	48	1898	76	−0.96
09QL-01 04	0.095076	0.003152	0.282305	0.000018	516	0.282274	−6.3	0.6	1419	53	1876	80	−0.91
09QL-01 05	0.038108	0.001217	0.282106	0.000019	746	0.282089	−7.7	0.7	1625	53	2143	85	−0.96
09QL-01 06	0.079583	0.002427	0.282277	0.000022	515	0.282254	−7.0	0.8	1430	65	1922	100	−0.93
09QL-01 07	0.005802	0.000165	0.282276	0.000018	510	0.282274	−6.4	0.6	1349	49	1882	79	−1.00
09QL-01 08	0.051826	0.001785	0.282258	0.000017	521	0.282240	−7.3	0.6	1434	48	1949	76	−0.95
09QL-01 09	0.049996	0.001810	0.282247	0.000017	738	0.282222	−3.2	0.6	1450	49	1852	77	−0.95
09QL-01 10	0.059872	0.002057	0.282021	0.000023	954	0.281985	−6.8	0.8	1783	64	2241	100	−0.94
09QL-01 11	0.034578	0.001176	0.282355	0.000021	743	0.282339	1.1	0.7	1274	59	1587	93	−0.96
09QL-01 12	0.042932	0.001514	0.282247	0.000017	767	0.282225	−2.4	0.6	1438	48	1825	76	−0.95
09QL-01 13	0.027738	0.001017	0.282298	0.000019	518	0.282288	−5.7	0.7	1349	54	1845	86	−0.97
09QL-01 14	0.050291	0.001785	0.282253	0.000017	754	0.282227	−2.6	0.6	1441	49	1829	77	−0.95
09QL-01 15	0.038172	0.001373	0.282134	0.000018	755	0.282115	−6.6	0.6	1592	50	2079	80	−0.96
09QL-01 16	0.052973	0.001842	0.282240	0.000017	515	0.282222	−8.1	0.6	1462	47	1994	74	−0.94
09QL-01 17	0.061743	0.002270	0.282201	0.000016	837	0.282165	−3.0	0.6	1535	46	1915	71	−0.93
09QL-01 18	0.044416	0.001649	0.282190	0.000018	744	0.282167	−5.0	0.6	1525	50	1970	79	−0.95
09QL-01 19	0.033773	0.001185	0.282173	0.000019	744	0.282156	−5.4	0.6	1530	52	1995	82	−0.96
09QL-01 20	0.037952	0.001378	0.282089	0.000019	748	0.282070	−8.4	0.7	1656	54	2184	85	−0.96
09QL-01 21	0.063700	0.002242	0.282345	0.000022	747	0.282314	0.3	0.8	1325	65	1640	100	−0.93
09QL-01 22	0.054447	0.001839	0.282245	0.000017	749	0.282219	−3.0	0.6	1454	47	1850	74	−0.94
09QL-03 01	0.046804	0.001608	0.282170	0.000017	705	0.282149	−6.5	0.6	1551	49	2035	78	−0.95
09QL-03 02	0.043897	0.001486	0.282233	0.000018	508	0.282219	−8.4	0.6	1457	52	2005	82	−0.96
09QL-03 03	0.012155	0.000358	0.282307	0.000017	512	0.282304	−5.3	0.6	1313	47	1814	77	−0.99
09QL-03 04	0.033331	0.001229	0.282249	0.000018	484	0.282238	−8.2	0.6	1425	52	1978	82	−0.96
09QL-03 05	0.102723	0.003926	0.282083	0.000021	496	0.282047	−14.8	0.7	1785	63	2395	92	−0.88
09QL-03 06	0.158327	0.005436	0.282197	0.000020	510	0.282145	−11.0	0.7	1686	63	2166	89	−0.84
09QL-03 07	0.016827	0.000565	0.282325	0.000014	516	0.282320	−4.7	0.5	1295	40	1776	64	−0.98
09QL-03 08	0.063730	0.002382	0.282275	0.000017	507	0.282252	−7.2	0.6	1432	50	1931	76	−0.93
09QL-03 09	0.060314	0.002270	0.282181	0.000022	504	0.282160	−10.6	0.8	1563	63	2139	98	−0.93
09QL-03 10	0.041527	0.001484	0.282231	0.000016	749	0.282210	−3.4	0.6	1461	45	1872	71	−0.96
09QL-03 11	0.011653	0.000464	0.282154	0.000017	515	0.282150	−10.7	0.6	1527	48	2155	77	−0.99
09QL-03 12	0.050122	0.001858	0.282253	0.000020	514	0.282235	−7.7	0.7	1443	57	1965	89	−0.94
09QL-03 13	0.057056	0.002150	0.282280	0.000019	508	0.282260	−7.0	0.7	1416	55	1914	86	−0.94
09QL-03 14	0.031725	0.001183	0.281659	0.000020	795	0.281641	−22.5	0.7	2245	56	3101	90	−0.96
09QL-03 15	0.052077	0.001903	0.282255	0.000014	735	0.282228	−3.0	0.5	1443	41	1839	63	−0.94
09QL-03 16	0.053806	0.001945	0.282171	0.000018	739	0.282144	−5.9	0.6	1565	52	2025	81	−0.94
09QL-03 17	0.066754	0.002456	0.282202	0.000018	509	0.282179	−9.8	0.6	1541	52	2094	80	−0.93
12QL-61 01	0.1552	0.0043	0.282499	0.000015	510	0.282458	0.1	0.5	1167	47	1474	34	−0.87
12QL-61 02	0.1789	0.0049	0.282474	0.000019	510	0.282427	−1.0	0.7	1230	58	1546	42	−0.85
12QL-61 03	0.2086	0.0057	0.282474	0.000021	510	0.282419	−1.2	0.8	1258	69	1562	48	−0.83

(*continued on next page*)

Table 6 (*continued*)

Sample	$^{176}Yb/^{177}Hf$	$^{176}Lu/^{177}Hf$	$^{176}Hf/^{177}Hf$	$\pm(2\sigma)$	$^{206}Pb/^{238}U$ Age (Ma)	$(^{176}Hf/^{177}Hf)_i$	$\varepsilon_{Hf}(t)$	$\pm(2\sigma)$	T_{DM1} (Ma)	$\pm(2\sigma)$	T_{DM2} (Ma)	$\pm(2\sigma)$	$f_{Lu/Hf}$
12QL-61 04	0.1496	0.0040	0.282423	0.000019	510	0.282385	−2.5	0.7	1273	58	1639	42	−0.88
12QL-61 05	0.1155	0.0031	0.282460	0.000018	510	0.282431	−0.8	0.6	1186	54	1537	41	−0.91
12QL-61 06	0.0701	0.0015	0.282441	0.000016	510	0.282426	−1.0	0.6	1165	47	1548	37	−0.95
12QL-61 07	0.1993	0.0052	0.282508	0.000027	510	0.282458	0.1	0.9	1186	85	1474	61	−0.84
12QL-61 08	0.0259	0.0006	0.282412	0.000015	510	0.282406	−1.7	0.5	1177	43	1592	35	−0.98
12QL-61 09	0.1457	0.0037	0.282550	0.000018	510	0.282514	2.1	0.6	1071	54	1348	40	−0.89
12QL-61 10	0.0502	0.0012	0.282383	0.000015	510	0.282372	−2.9	0.5	1234	42	1669	33	−0.97
12QL-61 11	0.1590	0.0045	0.282533	0.000019	510	0.282490	1.3	0.7	1122	59	1403	43	−0.87
12QL-61 12	0.1682	0.0048	0.282528	0.000017	510	0.282482	1.0	0.6	1141	52	1422	37	−0.85
12QL-61 13	0.1776	0.0050	0.282560	0.000020	510	0.282512	2.0	0.7	1096	64	1352	46	−0.85
12QL-61 14	0.1293	0.0037	0.282429	0.000020	510	0.282394	−2.1	0.7	1252	60	1618	45	−0.89
12QL-61 15	0.1816	0.0052	0.282556	0.000026	510	0.282506	1.8	0.9	1109	82	1366	58	−0.84
12QL-61 16	0.1045	0.0028	0.282455	0.000017	510	0.282428	−1.0	0.6	1185	49	1543	38	−0.92
12QL-61 17	0.1583	0.0047	0.282413	0.000017	510	0.282368	−3.1	0.6	1316	52	1677	38	−0.86
12QL-61 18	0.1200	0.0041	0.282427	0.000022	510	0.282389	−2.3	0.8	1269	66	1631	48	−0.88
12QL-61 19	0.1490	0.0046	0.282469	0.000018	510	0.282425	−1.0	0.6	1224	57	1549	41	−0.86
12QL-61 20	0.1481	0.0044	0.282382	0.000015	510	0.282340	−4.1	0.5	1352	47	1740	34	−0.87
12QL-61 21	0.1644	0.0049	0.282396	0.000022	510	0.282349	−3.8	0.8	1351	69	1721	49	−0.85
12QL-61 22	0.0353	0.0010	0.282380	0.000016	510	0.282370	−3.0	0.5	1234	44	1672	35	−0.97
12QL-61 23	0.0388	0.0011	0.282448	0.000014	510	0.282437	−0.6	0.5	1141	39	1522	31	−0.97
12QL-61 24	0.1124	0.0037	0.282373	0.000015	510	0.282338	−4.1	0.5	1337	44	1745	33	−0.89
12QL-61 25	0.0177	0.0005	0.282477	0.000014	510	0.282472	0.6	0.5	1083	39	1444	31	−0.98
12QL-61 26	0.1566	0.0046	0.282328	0.000019	510	0.282284	−6.0	0.7	1443	58	1866	42	−0.86
12QL-61 27	0.1820	0.0050	0.282399	0.000018	510	0.282351	−3.7	0.6	1349	56	1714	40	−0.85
12QL-61 28	0.0213	0.0005	0.282467	0.000015	510	0.282462	0.2	0.5	1097	43	1467	35	−0.98
12QL-61 29	0.0195	0.0005	0.282450	0.000014	510	0.282445	−0.3	0.5	1121	40	1505	32	−0.98
12QL-61 30	0.0198	0.0005	0.282468	0.000013	510	0.282463	0.3	0.5	1096	37	1464	30	−0.98

Note: $\varepsilon_{Hf}(0) = ((^{176}Hf/^{177}Hf)_S/(^{176}Hf/^{177}Hf)_{CHUR} - 1) \times 10{,}000$; $\varepsilon_{Hf}(t) = [(^{176}Hf/^{177}Hf)_S - (^{176}Lu/^{177}Hf)_S \times (e^{\lambda t} - 1)]/[(^{176}Hf/^{177}Hf)_{CHUR} - (^{176}Lu/^{177}Hf)_{CHUR} \times (e^{\lambda t} - 1) - 1] \times 10{,}000$; $T_{DM1} = 1/\lambda \times \ln 1 + [(^{176}Hf/^{177}Hf)_S - (^{176}Hf/^{177}Hf)_{DM}]/[(^{176}Lu/^{177}Hf)_S - (^{176}Lu/^{177}Hf)_{DM}]$; $T_{DM2} = T_{DM1} - (T_{DM1} - t) \times (f_{CC} - f_S)/(f_{CC} - f_{DM})$; $f_{Lu/Hf} = (^{176}Lu/^{177}Hf)_S/(^{176}Lu/^{177}Hf) - 1$, where $\lambda = 1.865 \times 10^{-11}$ year^{-1} (Scherer et al., 2001); $(^{176}Hf/^{177}Hf)_S$ and $(^{176}Lu/^{177}Hf)_S$ are the measured values of the samples; $(^{176}Hf/^{177}Hf)_{CHUR} = 0.282772$ and $(^{176}Lu/^{177}Hf)_{CHUR} = 0.0332$ (Blichert-Toft and Albarède, 1997); $(^{176}Hf/^{177}Hf)_{DM} = 0.28325$ and $(^{176}Lu/^{177}Hf)_{DM} = 0.0384$ (Griffin et al., 2000); $(^{176}Lu/^{177}Hf)_{mean\ crust} = 0.015$; $f_{CC} = [(^{176}Lu/^{177}Hf)_{mean\ crust}/(^{176}Lu/^{177}Hf)_{CHUR}] - 1$; $f_S = f_{Lu/Hf}$; $f_{DM} = [(^{176}Lu/^{177}Hf)_{DM}/(^{176}Lu/^{177}Hf)_{CHUR}] - 1$; t = crystallization time of zircon.

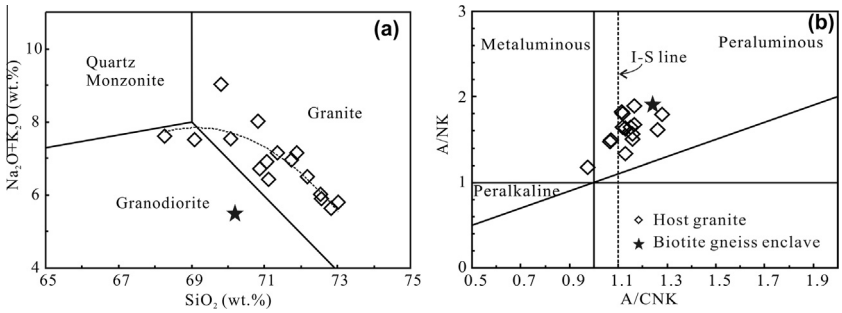

Fig. 3. Plots of $Na_2O + K_2O$ versus SiO_2 (a) and A/NK versus A/CNK (b). The I–S dashed line in (b) is after Chappell and White (2001).

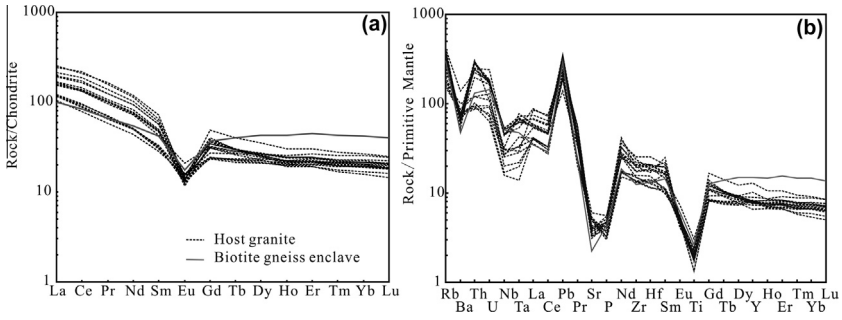

Fig. 4. Chondrite-normalized REE element pattern and primitive-mantle normalized trace element spidergrams for the Chaidanuo batholith. Normalization values are from Sun and McDonough (1989).

1096–1443 Ma, much younger than those of the host granite.

4.5. Crystallization temperature of the Chaidanuo granite

The minimum and maximum crystallization temperature attained by the zircon-saturated Chaidanuo granitic magma can be estimated by using methods of Ti-in-zircon thermometer and zircon saturation thermometer, respectively (Watson and Harrison, 1983, 2005; Hanchar and Watson, 2003; Miller et al., 2003; Bea et al., 2007; Ferry and Watson, 2007). It should be noted that data points with remarkably high Ti abundance in zircons have been excluded. We use the Ti-in-zircon thermometer from Ferry and Watson (2007) and a recommended value ($\alpha TiO_2 = 0.6$) for the activity of TiO_2 in rutile-free granitoids. Calculated Ti-in-zircon temperatures for the 516–510-Ma zircons give an average value of 790 ± 58 °C ($N = 17$). A mean zircon saturation temperature of 814 ± 18 °C ($N = 21$) is acquired from whole-rock compositions of the host granite (Table 2). Therefore, the Chaidanuo peraluminous granite was crystallized at a temperature range of 814–790 °C.

5. PETROGENESIS OF THE CHAIDANUO PERALUMINOUS GRANITE

5.1. Metamorphism/melting of the upper continental crust at 516–503 Ma

Abundant inherited cores of zircons from the host granite record a dominant peak of magmatic age at ~750 Ma with minor magmatic/metamorphic ages dispersed from 591 to 1683 Ma. Both assimilation of country-rocks and incomplete melting of source rocks can explain the inherited zircon cores in the host granite. However, the fairly homogeneous Nd isotopic compositions [$\varepsilon_{Nd}(t) = -6.0$ to -7.1] of the host granite and comparable Hf isotopic compositions between the inherited zircon cores [$\varepsilon_{Hf}(t = 510\ Ma) = -16.0$ to -0.4] and the 516–510 Ma zircon rims [$\varepsilon_{Hf}(t = 510\ Ma) = -14.5$ to -4.8] suggest that the wall-rock assimilation, if any, is insignificant (Fig. 7a). As shown in Fig. 7b, inherited zircons share a close affinity in two-stage model ages (peaking at ~1952 and ~2155 Ma) with the 516–510 Ma zircons (peaking at ~1853, 2022 and ~2183 Ma). The less variable $\varepsilon_{Hf}(t)$ values in the rims than in the cores of the 510 Ma-aged zircons may be due to Hf isotopic homogenization that occurred within the granitic melt during partial melting (Wu et al., 2007). The Paleoproterozoic weighted mean T_{DM2} age of 1974 ± 74 Ma for the 516–510 Ma zircons implies that their protolith formed by reworking of ancient crust. In spite of an age peak of ~750 Ma in detrital zircon age spectra of some Qilian sediments, melting of a sediment-dominated source is unlikely as it will also introduce other age peaks such as ~2.5, ~1.6, ~1.0 Ga and so on (Yang et al., 2009; Xu et al., 2010). Therefore, these inherited zircons most likely originated from igneous source rocks of the Chaidanuo granite, which indicates the involvement of ~750 Ma igneous rocks with minor sediments in the Paleoproterozoic crust for the generation of Chaidanuo granite.

Inherited cores of zircons from the biotite gneiss enclave record a magmatic protolith age of 744 ± 10 Ma, indicating the biotite gneiss enclave was derived from the ~744 Ma

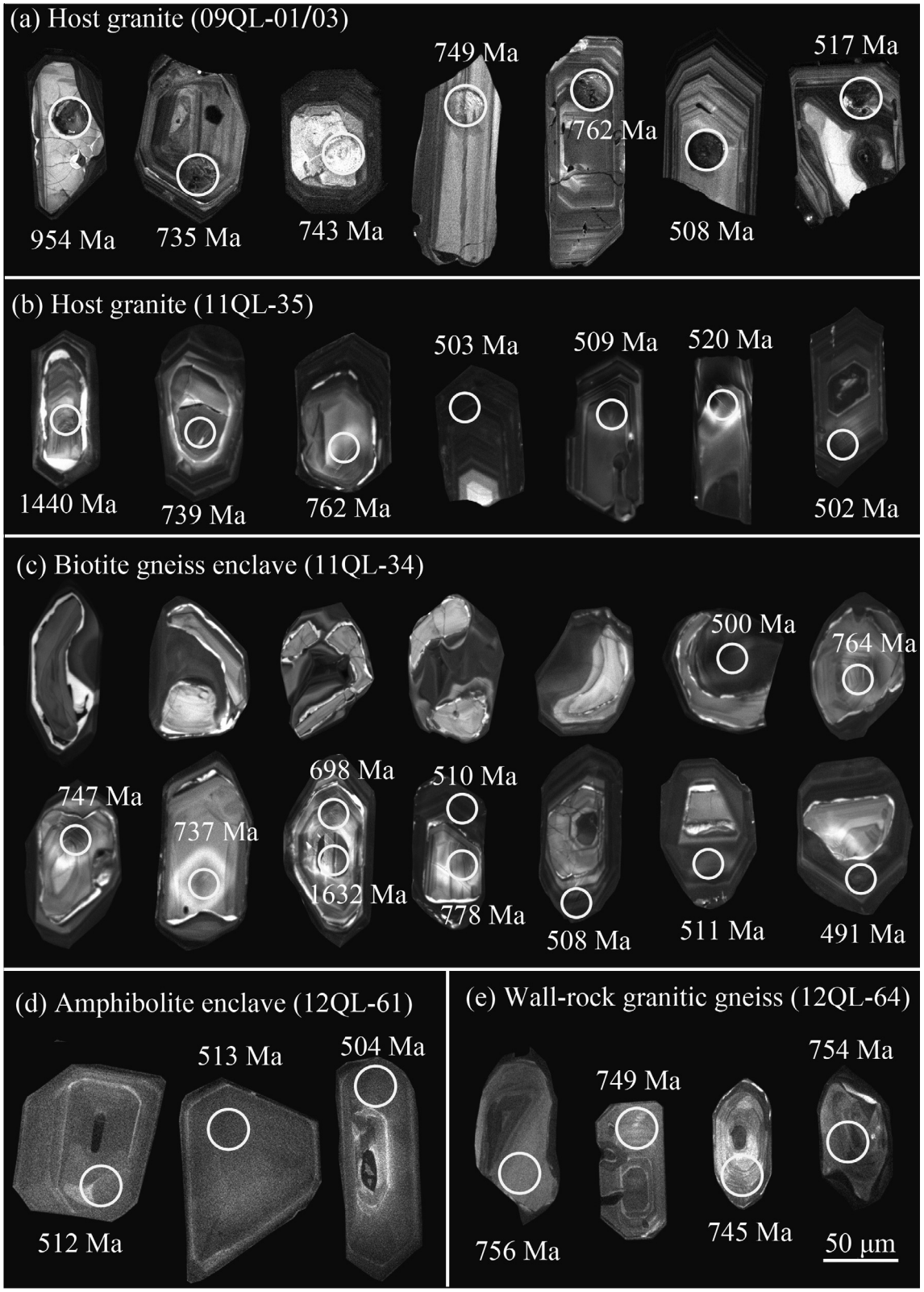

Fig. 5. Representative CL images of zircon grains showing spots for zircon LA-ICP-MS (big circle), SIMS (small circle) U–Pb and LA-MC-ICP-MS Lu–Hf analyses. See detailed description in the text.

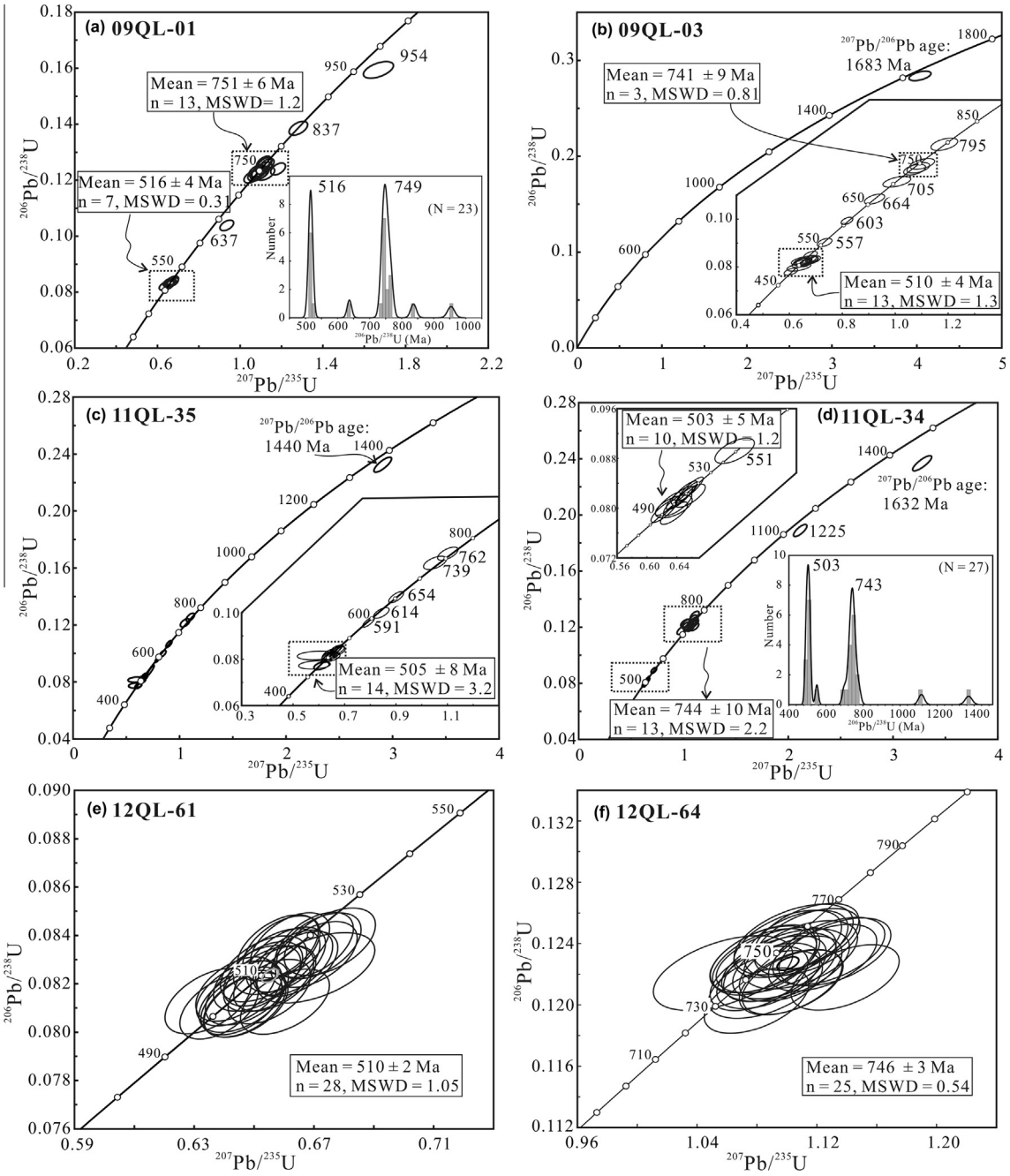

Fig. 6. Concordia diagrams of U–Pb zircon age data for the host biotite monzogranite (09QL-01, 09QL-03 and 11QL-35), biotite gneiss enclaves (11QL-34), mafic magmatic enclaves (12QL-61) and the granitic country rocks (12QL-64). (a), (b), (e) and (f) by LA-ICP-MS; (c) and (d) by SIMS. (a)–(c) Showing that the Chaidanuo granite was crystallized at an age span of 516–505 Ma with inherited ages from 591 to 1683 Ma peaking at ~750 Ma; (d) the biotite gneiss enclaves recording a magmatic protolith age of ~744 Ma, indistinguishable from the 746 Ma wall-rock granitic gneiss (e), and a metamorphic/anatexis overprinting at ~503 Ma; (f) mafic magmatic enclaves crystallized at ~510 Ma.

granite. The granite protolith may belong to S-type based on its geochemical features [e.g., high K_2O content (Fig. 10), strongly peraluminous (Fig. 3b) and enriched Sr–Nd isotopes (Fig. 8)]. Meta-sedimentary and granitic gneiss enclaves are common in granitoids of crustal origin and can be either xenoliths captured from country rocks by magmas en route to the surface, or restites representing remnants of their source rocks (Chen et al., 1989; Didier and Barbarin, 1991; White et al., 1999; Clemens, 2003; Chappell and Wyborn, 2012). Biotite gneiss enclaves and biotite aggregates in the Chaidanuo batholith are relatively rare and have variable biotite modal contents (Fig. 2H and I); the red-brown biotite aggregates may be remnants of partly melted source rocks (Fig. 2I), but biotite gneiss

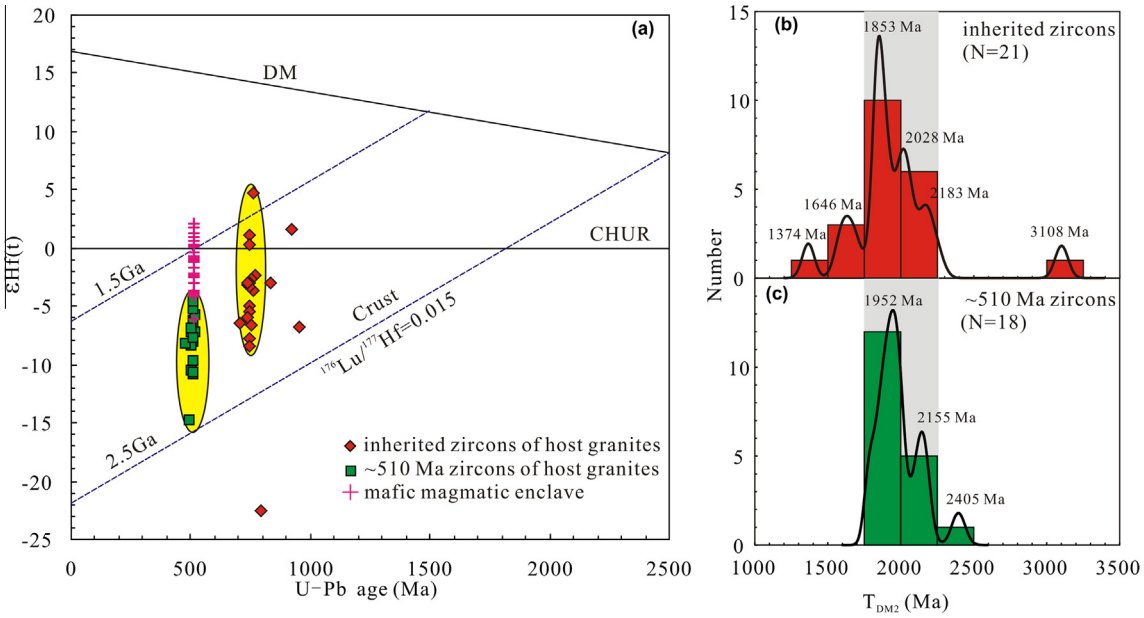

Fig. 7. Plot of $\varepsilon_{Hf}(t)$ values versus U–Pb ages of zircons from the host granites and mafic magmatic enclave (a), histograms of T_{DM2} for the inherited (b) and ~510 Ma (c) zircons from the host granites.

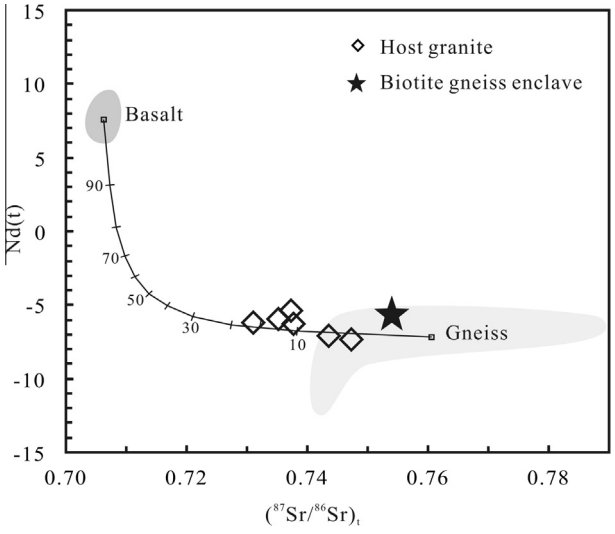

Fig. 8. Plot of ε_{Nd} ($t = 510$ Ma) versus ($^{87}Sr/^{86}Sr$)i for the host biotite monzogranites and biotite gneiss enclave in the NQOB. Data for basalts are from the Dachadaban lower tholeiite terrane in the NQOB (Zhang et al., 1998) and Gneiss from Xu (2007). The mixing line was calculated after Zou (2007).

enclaves (e.g., sample 11QL-34) are compositionally felsic and lack refractory mineral phases, and thus do not seem to be residues (Fig. 2H) (Didier and Barbarin, 1991; Clemens, 2003). Nevertheless, zircons from the biotite gneiss enclave record a magmatic protolith age of 744 ± 10 Ma and a metamorphic/anatectic overprinting at 503 ± 5 Ma. The 744-Ma protolith age is in agreement with the major population of 750-Ma inherited zircons from the host granites and the 746-Ma magmatic age of the wall-rock granitic gneiss. These, combined with the 776–751 Ma granitic gneisses (Su et al., 2004; Tseng et al., 2006) and the ~753 Ma peak in detrital zircons from sediments (Xia, 2012), suggest the presence of Neoproterozoic granitoids in the upper continental crust of the NQOB. The 503-Ma metamorphic/anatectic age in the biotite gneiss enclave is the same within errors as the crystallization age of the granite host (505 ± 8 Ma). CL images (Fig. 5c) show that most protolith zircons (i.e., core domains) are strongly melting-corroded and recrystallized at conditions above solidus, indicating derivation of biotite gneiss enclaves from mid-crustal levels either within or slightly above the source region of the host granite (e.g., Chen et al., 1989; Maas et al., 2001). This establishes the timing of the metamorphism/anatectic event of the continental crust at 516–503 Ma and an essential link between remelting of ~750 Ma S-type granitic rocks and formation of the Chaidanuo granite. In other words, the biotite gneiss enclaves must be residue/restite (possibly "resistate" as per Vernon, 2007) from partial melting of the upper continental crust, which is further supported by evidence including Nd isotopes and whole-rock chemical compositions:

(1) The Nd isotopic compositions [$\varepsilon_{Nd}(t) = -6.0$ to -7.1] of the Chaidanuo peraluminous granites overlap values of the biotite gneiss enclave in this study and felsic gneisses [$\varepsilon_{Nd}(t) = -6.3$ to -10.8] in the Qilian Precambrian basement (Xu, 2007) (Fig. 8).
(2) The striking Th, U and Pb peaks and Nb, Ta, Ti, Sr and Eu troughs in Fig. 4b directly reflect that the parental magma of Chaidanuo batholith is characteristic of melts derived from upper crust (Rudnick and Gao, 2003). The Chaidanuo peraluminous granites have high CaO/Na_2O (>0.3) but low Rb/Ba and Rb/Sr ratios (Fig. 9a and b), indicating an origin

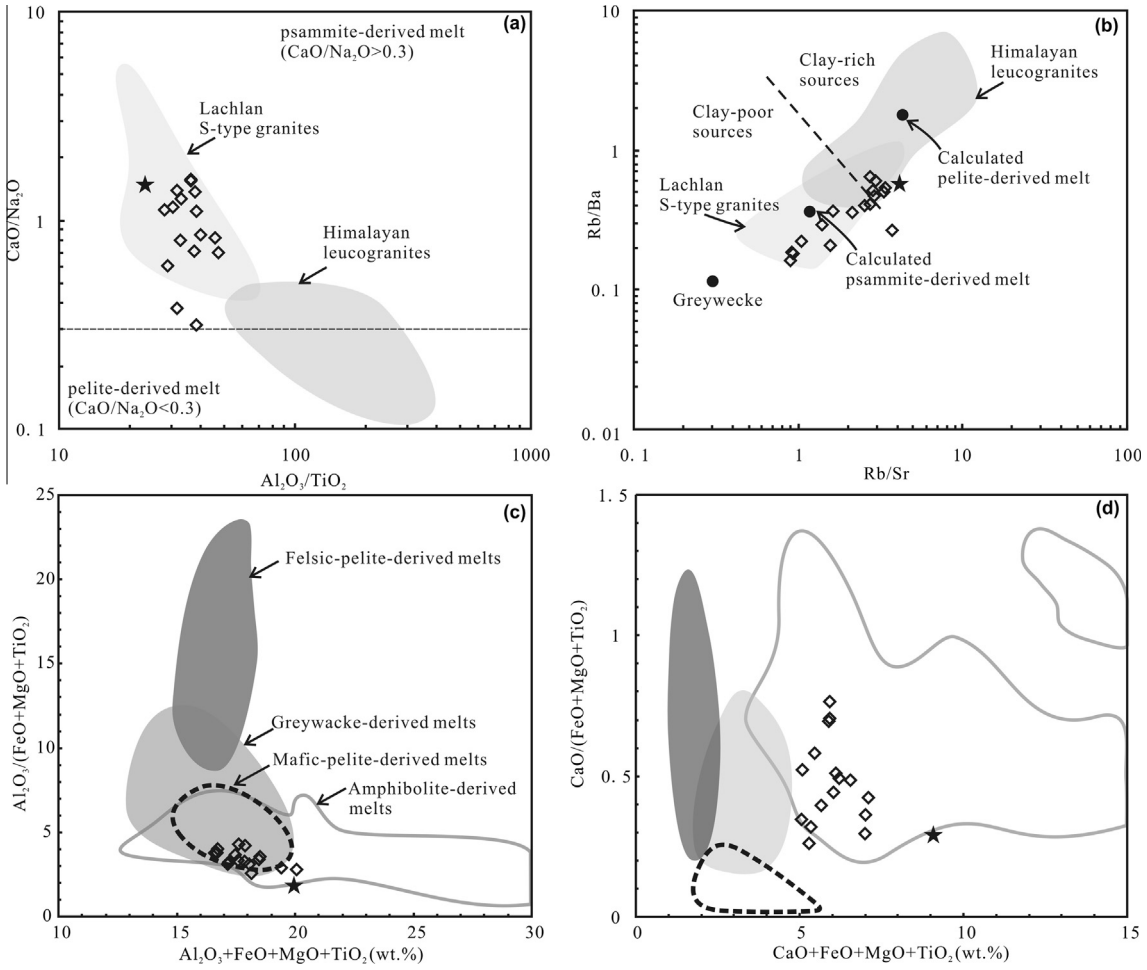

Fig. 9. Plots of Al_2O_3/TiO_2 versus CaO/Na_2O (a), Rb/Sr versus Rb/Ba (b), $Al_2O_3 + FeO + MgO + TiO_2$ versus $Al_2O_3/(FeO + MgO + TiO_2)$ (c) and $CaO + FeO + MgO + TiO_2$ versus $CaO/(FeO + MgO + TiO_2)$ (d) of the Chaidanuo batholith. Data sources: (a) and (b), the Himalayan leucogranites (Searle and Fryer, 1986; Inger and Harris, 1993; Ayres and Harris, 1997) and the Lachlan S-types granites (Chappell and Simpson, 1984; Healy et al., 2004); (c) and (d) are after Patiño Douce (1999). Symbols as in Fig. 8.

from partial melting of plagioclase-rich and clay-poor sources that can be either psammite (e.g., similar to the Lachlan S-type granite) or orthogneiss with similar mineralogy (Sylvester, 1998). However, the spatial and temporal association of the Chaidanuo granite with the 744 Ma orthogneiss resistates and 746 Ma country-rocks implies that a ~750 Ma S-type granitoid is the major source, very different from the Lachlan S-type granite that is tightly associated with sedimentary country rocks and high-grade meta-sedimentary enclaves from mid-crustal levels (e.g., Chen et al., 1989; Maas et al., 2001). Thus, large scale melting of continental crust, including ~750 Ma granitic rocks and minor clay-poor sediments, seems likely to be responsible for the generation of the Chaidanuo peraluminous granite.

5.2. Contributions of mantle and magma mixing

Several mechanisms, such as fractional crystallization, restite unmixing or magma mixing, have been proposed to explain the origin of MMEs in granitoid intrusions (e.g., Barbarin, 2005; Yang et al., 2007; Chappell and Wyborn, 2012). The MME sample (510 ± 2 Ma) shows similar crystallization age but its zircons are more depleted $\varepsilon_{Hf}(t)$ values (−6.0 to +2.1) than ~510-Ma-aged zircons (−14.8 to −4.7) of the host granite, ruling out the possibility of fractional crystallization or restite unmixing. Inherited zircon cores are abundant in the host granite but rare in the MME, which further argue against a restitic origin for the MMEs (Fig. 6a–c, e). Coeval arc basaltic rocks and subduction-related I-type granitoids near the studied area indicate contemporary mantle-derived magmatism (Zhang et al., 1997; Wu et al., 2010; Xia et al., 2012; Song et al., 2013). Although the highest $\varepsilon_{Hf}(t)$ value (+2.1) is significantly lower than that of the depleted mantle (Fig. 7), mixing between depleted mantle-derived mafic magma and crustal-derived felsic magmas can lower and result in variable $\varepsilon_{Hf}(t)$ values (Yang et al., 2007), which is the case for the MME (−6.0 to +2.1). Thus, the MMEs probably represent derivatives of depleted mantle-derived mafic magmas intruding partially crystallized crust-derived felsic magmas (Barbarin, 2005).

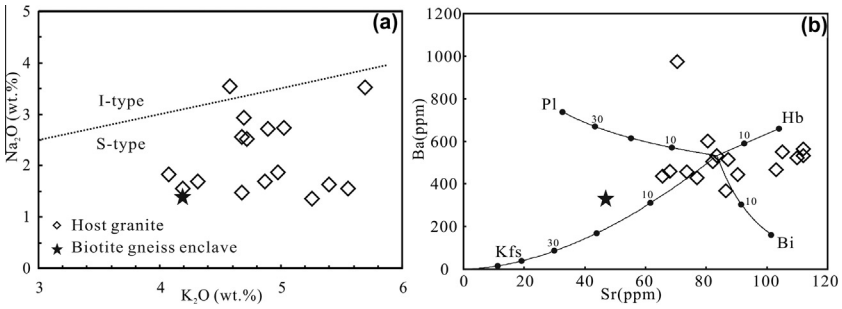

Fig. 10. Plots of Na_2O versus SiO_2 (a) and Ba versus Sr (b) for the Chaidanuo batholith. The I–S line in (a) is after Chappell and White (2001); (b) showing that geochemical variations in the Chaidanuo granite could not be controlled by fractionation of feldspar or/and biotite. Partition coefficients of Sr and Ba are from Rollison (1993). Plag: Plagioclase; Hbl: Hornblende; Ksp: K-feldspar, Bi: Biotite.

Similar to the Lalchan S-type granites, the Chaidanuo peraluminous granites have lower Al_2O_3/TiO_2 values than the Himalayan leucogranites, ascribed to breakdown of biotite rather than muscovite at a relatively high temperature (Fig. 9a) (Sylvester, 1998; Patiño Douce, 1999). This is in accordance with the relatively high crystallization temperature (~814–790 °C) of the host granite and presence of biotite as the unique mafic mineral in the host granite and biotite gneiss resistates. It is notable that the continental crust can hardly reach such a high temperature for dehydration melting of biotite without additional source of heat, for example, underplating of mantle-derived magma (Patiño Douce, 1999). In the case of the Chaidanuo peraluminous granites, mantle-derived magma may contribute both heat and material. The restite-unmixing/one-component model fails to explain the overall higher FeO and MgO abundances than experimental melts from metagreywacke (psammite), thus causing the Chaidanuo granites projecting away from the metagreywacke field but within amphibolite field (Fig. 9c and d). This, together with the Sr isotopic discrepancy between the Chaidanuo granites ($I_{Sr}(t) = 0.7310$–0.7436) and the granitic gneiss component ($I_{Sr}(t) = 0.7434$–0.7882), requires an additional mafic component with depleted $I_{Sr}(t)$ (<0.731). The coeval MMEs provide convincing evidence of injection of mantle-derived magma into the Chaidanuo peraluminous melt, resembling peraluminous granites of hybrid origin world-wide (Keay et al., 1997; Collins, 1998; Healy et al., 2004; Yang et al., 2007; Cai et al., 2011). For Sr–Nd isotopic modeling, the 517-Ma Dachadaban tholeiite (Zhang et al., 1998; Xia et al., 2012) was chosen as the mafic component because of the close relationship with the Chaidanuo granite in space and time, and a maximum input of 10–18% mantle-derived magma is required (Fig. 8).

In summary, the Chaidanuo peraluminous granite represents considerable in situ melting of the upper continental crust that is dominated by the Neoproterozoic granitic rocks and minor sediments due to the addition material and heat from enriched mantle-derived magma.

5.3. Petrogenetic type: I-, S- or others?

Based on previous studies, generation of peraluminous, silica-rich melts could be summarized as: (1) fractional crystallization of less aluminous phase from metaluminous melts (Wu et al., 2003a,b); (2) dehydration-melting of quartz amphibolite (Patiño Douce and Beard, 1995); (3) vapor-absent or water-saturated melting of alumina-rich metapelite or/and metagreywacke (Breton and Thompson, 1988; Vielzeuf and Holloway, 1988; Patiño Douce and Johnston, 1991;Vielzeuf and Montel, 1994; Gardien et al., 1995, 2000; Patiño Douce and Beard, 1995; Montel and Vielzeuf, 1997; Patiño Douce, 1999); and (4) partial melting of mixed meta-sediments and basaltic rocks (Skjerlie et al., 1993; Patiño Douce, 1995; Cai et al., 2011).

Compared with experimental quartz-amphibolite-derived melts (Patiño Douce and Beard, 1995), the Chaidanuo peraluminous granite is CaO-poor and K_2O-rich. Compared to highly fractionated I-type granites in previous studies (Chappell, 1999; Wu et al., 2003a), the Chaidanuo granite has a relatively narrow range of SiO_2 (69.6–74.4 wt%) and is Na_2O-poor (mostly <3 wt.% except two samples), K_2O-rich (most >4 wt.%) and ASI mostly >1.1 (Figs. 3b and 10a). The co-variation between Sr and Ba in the Chaidanuo granite (Fig. 10b) also suggests that fractional crystallization is insignificant, although the weakly negative trends of Fe_2O_3t, MgO, TiO_2, Na_2O, Al_2O_3, P_2O_5 and total alkai contents against SiO_2 seem to be caused by separation of a small amount of biotite, feldspar, Fe–Ti oxides, and apatite (Figs. 3a and 11a–e).

Preservations of supracrustal xenoliths, biotite gneiss resistates and abundant inherited/detrital zircon cores in the Chaidanuo granite are important features that are commonly seen in S-type granites (Clemens, 2003). As shown in Fig. 10a, the Chaidanuo granites show similar Na_2O and K_2O contents with S-type granites. Similar to S-type granites, irregular changes of K_2O, CaO, Rb, and Mg# (not shown) with increasing SiO_2 cannot be simply explained by fractionation process or progressive partial melting, but may imply source heterogeneity, ineffective removal of restites, selective entrainment of peritectic minerals like garnet (Stevens et al., 2007) or magma mixing. However, the Chaidanuo granite lacks characteristic Al-rich minerals such as muscovite, garnet, cordierite, sillimanite, and so on. Instead, biotite is the unique mineral phase that is strongly peraluminous and it accounts for the whole-rock peraluminous signature in both the Chaidanuo granite and biotite gneiss resistates. As stated above, the Chaidanuo peraluminous

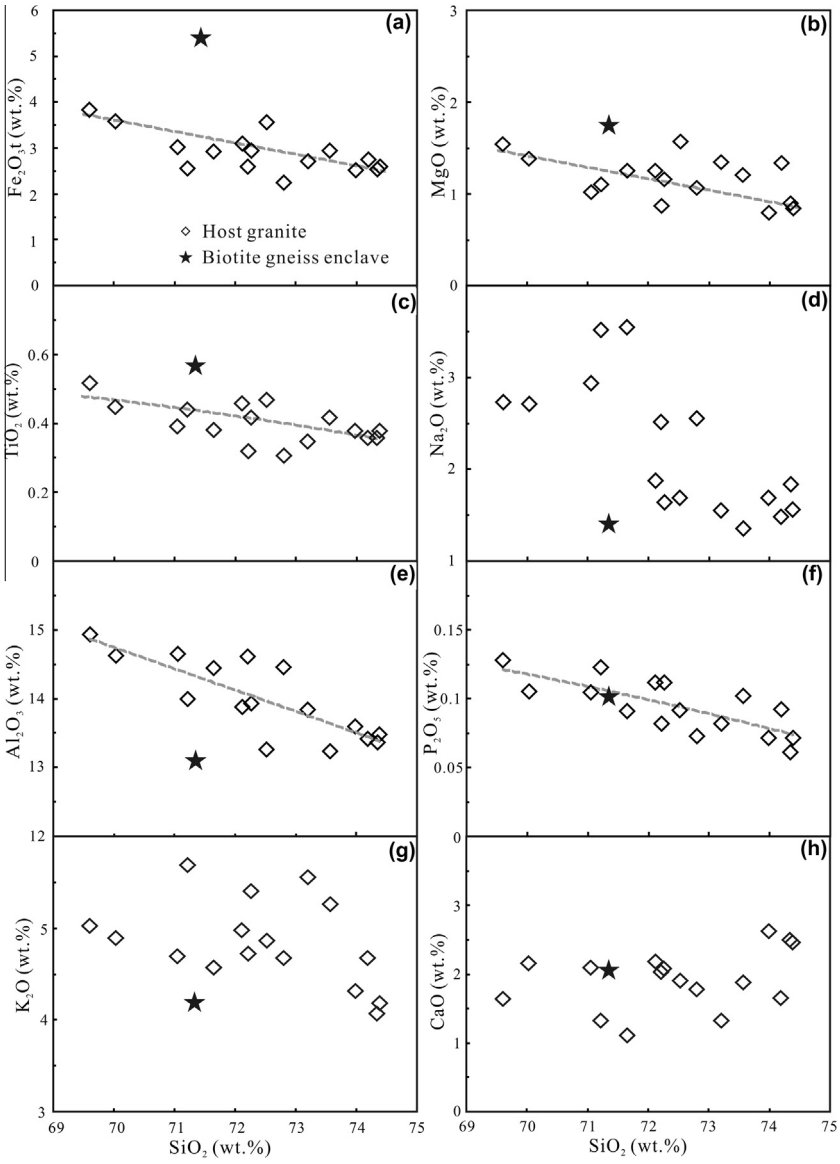

Fig. 11. Harker diagrams showing variation of other major element oxides versus SiO_2 for the Chaidanuo granites and biotite gneiss enclave.

granite is mainly derived from melting of upper continental crust with mixing of minor mantle-derived magma. Thus, the Chaidanuo peraluminous granite is better considered as transitional between I- and S-type granites.

6. SUBDUCTION INITIATION AND RECYCLING OF UPPER CONTINENTAL CRUST

The ridge subduction model for the genesis of the peraluminous granite is unlikely the case in the NQOB because the HP/LT metamorphic rocks suggest a cold seafloor subduction with a low geothermal gradient (6–7 °C/km) (Wu et al., 1993; Song et al., 2007, 2009a; Zhang et al., 2007). Other tectonic models, such as crustal thickening during continental collision, post-collisional collapse and melting of pre-existed sediments in the back-arc basin during its extension caused by repeated slab-roll back (Sylvester, 1998; Barbarin, 1999; Collins, 2002; Collins and Richards, 2008), also cannot account for the origin of the Chaidanuo granite because of the age constraints. The age (516–505 Ma) of the Chaidanuo batholith emplacement is older than the ages of back-arc-basin ophiolites (490–448 Ma) and eclogites (490–460 Ma), but contemporaneous with the lower tholeiitic part of the Dachadaban boninite massif (517–505 Ma), subduction-related I-type granitoids (512–476 Ma) in the NQOB (Wu et al., 2010; Xia and Song, 2010; Xia et al., 2012; Song et al., 2013) and the MME (510 Ma) in this study,, indicating a genetic relationship between mantle upwelling during subduction initiation and generation of the Chaidanuo peraluminous granite.

Subduction nucleation at a passive margin was widely accepted as the direct consequence of growing negative buoyancy of the oceanic plate because it became older and colder as it migrated away from ocean ridges, although

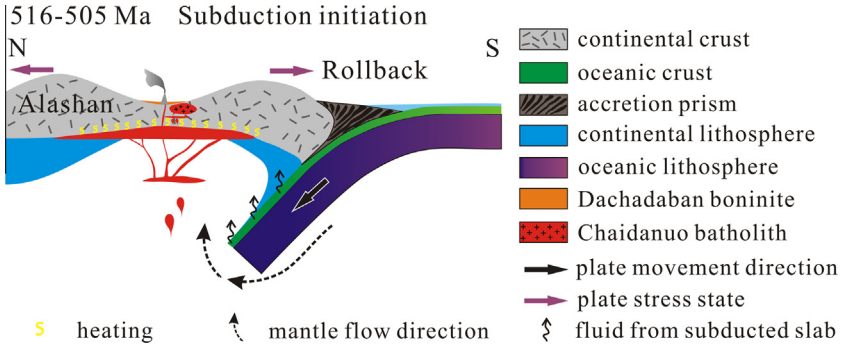

Fig. 12. Schematic diagram illustrating underplating of upwelling-mantle-derived magma by trench rollback into the Qilian continental arc during subduction initiation and melting of upper continental crust to generate the Chaidanuo granitoids.

additional geodynamic forces favoring subduction initiation such as rifting, thermal-chemical plume ascent or/and sedimentary loading were also proposed (Niu et al., 2003; Gerya, 2011; Nikolaeva et al., 2011). Passive continental margin failure seems to be preceded by an overthrusting period during which the continental crust crept over the oceanic crust and oceanic lithosphere delaminated from the continental lithosphere afterwards (Mart et al., 2005; Goren et al., 2008; Nikolaeva et al., 2010, 2011). Once subduction has initiated, a strong slab rollback towards vertical increases subduction rate (see Figs. 4 and 5 of Niu et al., 2003) and intense seafloor spreading would be expected (Hall et al., 2003; Gorczyk et al., 2007; Nikolaeva et al., 2008; Zhu et al., 2009; Gerya, 2011). As a result, trench retreat and extension of the overriding plate locally occur, for example, in the fore-arc region. The overriding plate can be rheologically weakened by arc magmatism, which causes thinning of the overriding plate (Nikolaeva et al., 2008; Gerya and Meilick, 2011). This process will induce decompression melting of asthenosphere mantle (Hall et al., 2003; Gorczyk et al., 2007; Gerya et al., 2008) and simultaneously produces basaltic magmatism atop the dipping slab, i.e., the fore-arc basalts and subsequent boninites such as in the Izu-Bonin-Mariana intra-oceanic arc system (Ishizuka et al., 2011). The Dachadaban boninite complex convincingly enhances the likelihood of decompression melting of asthenosphere mantle in the onset of subduction (Xia et al., 2012). Consequently, the overriding continental crust is deemed to suffer from heating when underplated with mantle-derived magmas, and will begins to melt once temperature reaches the solidus. The late Paleozoic peraluminous granitoids in central Chile might be one natural example, which reveal nearly 30–80% melting of recycled continental crust during subduction initiation on the basis of geochemical and numerical modeling (Lucassen et al., 2004; Gorczyk et al., 2007). As a batholith that represents mixed product of 82–90% upper continental crust-derived and 10–18% mantle-derived magmas, it is reasonable to infer that large scale melting of upper continental crust triggered by mantle upwelling during subduction initiation produced the melt that formed the ~500-km^2 Chaidanuo peraluminous granitic batholith (Fig. 12). The mantle-derived mafic magma broke up into blobs and was scatter in the partially crystallized Chaidanuo granite to form MME (Barbarin, 2005).

7. CONCLUSIONS

1. The Chaidanuo peraluminous granite was formed in a period of 516–505 Ma, coeval with the earliest arc magmatism in the NQOB.
2. Petrology, whole-rock major element, trace element and Sr–Nd isotope geochemistry, and zircon U–Pb–Hf isotopes all consistently suggest that the Chaidanuo peraluminous granite is largely generated by melting of the upper continental crust with the injection of 10–18% mantle-derived basaltic magma.
3. Large scale melting and continental crust recycling can occur at the early stage of seafloor subduction. As the subduction initiates, local extension of the overriding continental plate as a result of trench rollback triggers asthenosphere upwelling to produce mantle-derived basaltic magma, which then facilitated extensive melting of the upper continental crust.

ACKNOWLEDGMENTS

This study was supported by National Natural Science Foundation of China (Grant Nos. 41372060, 40825007, 41121062, 41130314), Basic geological survey program of China Geological Survey (1212011121258) and the Major State Basic Research Development Projects (2009CB825007). We thank L. Su for helping with whole-rock analyses and LA-ICP-MS dating, X.H. Li, Y. Liu and Y.F. Wang for SIMS dating, K.J. Hou and C.L. Guo for MC-ICP-MS in-situ zircon Hf analyses, and G.Z. Li and W.P. Zhu for Sr–Nd isotopic analyses. We also thank three anonymous reviewers and editors for their detailed and constructive comments, which make presentation of the final product.

REFERENCE

Ague J. J. and Brimhall G. H. (1987) Granites of the batholiths of California: products of local assimilation and regional-scale crustal contamination. *Geology* **15**, 63–66.

Andersen T. (2002) Correction of common lead in U–Pb analyses that do not report ^{204}Pb. *Chem. Geol.* **192**, 59–79.

Ayres M. and Harris N. (1997) REE fractionation and Nd-isotope disequilibrium during crustal anatexis: constraints from Himalayan leucogranites. *Chem. Geol.* **139**, 249–269.

Barbarin B. (1996) Genesis of the two main types of peraluminous granitoids. *Geology* **24**, 295–298.

Barbarin B. (1999) A review of the relationships between granitoid types, their origins and their geodynamic environments. *Lithos* **46**, 605–626.

Barbarin B. (2005) Mafic magamtic enclaves and mafic rocks associated with some granitoids of the central Sierra Nevada batholith, California: nature, origin, and relations with the hosts. *Lithos* **80**, 155–177.

Bea F., Montero P., González-Lodeiro F. and Talavera C. (2007) Zircon inheritance reveals exceptionally fast crustal magma generation processes in Central Iberia during the Cambro-Ordovician. *J. Petrol.* **48**, 2327–2339.

Black L. P., Kamo S. L., Allen C. M., Aleinikoff J. N., Davis D. W., Korsch R. J. and Foudoulis C. (2003) TEMORA 1: a new zircon standard for Phanerozoic U–Pb geochronology. *Chem. Geol.* **200**, 155–170.

Blichert-Toft J. and Albarède F. (1997) The Lu–Hf isotope geochemistry of chondrites and the evolution of the mantle-crust system. *Earth Planet. Sci. Lett.* **148**, 243–258.

Breton N. L. and Thompson A. B. (1988) Fluid-absent (dehydration) melting of biotite in metapelites in the early stages of crustal anatexis. *Contrib. Miner. Petrol.* **99**, 226–237.

Cai K. D., Sun M., Yuan C., Zhao G. C., Xiao W. J., Long X. P. and Wu F. Y. (2011) Geochronology, petrogenesis and tectonic significance of peraluminous granites from the Chinese Altai, NW China. *Lithos* **127**, 261–281.

Chappell B. W. (1999) Aluminium saturation in I- and S-type granites and the characterization of fractionated haplogranites. *Lithos* **46**, 535–551.

Chappell B. W. and Simpson P. R. (1984) Source rocks of I- and S-type granites in the lachlan fold belt, Southeastern Australia [and discussion]. *Phil. Trans. Roy. Soc. London A Math. Phys. Sci.* **310**, 693–707.

Chappell B. W. and White A. J. R. (1974) Two contrasting granite types. *Pacific Geol.* **8**, 173–174.

Chappell B. W. and White A. J. R. (2001) Two contrasting granite types: 25 years later. *Aust. J. Earth Sci.* **48**, 489–499.

Chappell B. W. and Wyborn D. (2012) Origin of enclaves in S-type granites of the Lachlan Fold Belt. *Lithos* **154**, 235–247.

Chen Y. D., Price R. C. and White A. J. R. (1989) Inclusions in three S-type granites from Southeastern Australia. *J. Petrol.* **30**, 1181–1218.

Chen Y. D., Price R. C., White A. J. R. and Chappell B. W. (1990) Mafic inclusions from the Glenbog and Blue Gum granite suites, Southeastern Australia. *J. Geophys. Res.* **95**, 17757–17785.

Clemens J. D. (2003) S-type granitic magmas-petrogenetic issues, models and evidence. *Earth Sci. Rev.* **61**, 1–18.

Collins W. J. (1998) Evaluation of petrogenetic models for Lachlan Fold Belt granitoids: implications for crustal architecture and tectonic models. *Aust. J. Earth Sci.* **45**, 483–500.

Collins W. J. (2002) Hot orogens, tectonic switching, and creation of continental crust. *Geology* **30**, 535–538.

Collins W. J. and Richards S. W. (2008) Geodynamic significance of S-type granites in circum-Pacific orogens. *Geology* **36**, 559–562.

Dan W., Li X. H., Guo J. H., Liu Y. and Wang X. C. (2012) Paleoproterozoic evolution of the eastern Alxa Block, westernmost North China: evidence from in situ zircon U–Pb dating and Hf–O isotopes. *Gondwana Res.* **21**, 838–864.

Didier J. and Barbarin B. (1991) *Enclaves and Granite Petrology*. Elsevier Science Publishers B.V., New York.

Ferry J. and Watson E. (2007) New thermodynamic models and revised calibrations for the Ti-in-zircon and Zr-in-rutile thermometers. *Contrib. Miner. Petrol.* **154**, 429–437.

Frost B. R., Barnes C. G., Collins W. J., Arculus R. J., Ellis D. J. and Frost C. D. (2001) A geochemical classification for granitic rocks. *J. Petrol.* **42**, 2033–2048.

Gardien V., Thompson A. B., Grujic D. and Ulmer P. (1995) Experimental melting of biotite + plagioclase + quartz ± muscovite assemblages and implications for crustal melting. *J. Geophys. Res.* **100**, 15581–15591.

Gardien V., Thompson A. B. and Ulmer P. (2000) Melting of biotite + plagioclase + quartz gneisses: the role of H_2O in the stability of amphibole. *J. Petrol.* **41**, 651–666.

Gaschnig R. M., Vervoort J. D., Lewis R. S. and Tikoff B. (2011) Isotopic evolution of the Idaho batholith and Challis Intrusive Province, Northern US Cordillera. *J. Petrol.* **52**, 2397–2429.

Gerya T. V. (2011) Future directions in subduction modeling. *J. Geodyn.* **52**, 344–378.

Gerya T. V. and Meilick F. I. (2011) Geodynamic regimes of subduction under an active margin: effects of rheological weakening by fluids and melts. *J. Metamorph. Geol.* **29**, 7–31.

Gerya T. V., Connolly J. A. D. and Yuen D. A. (2008) Why is terrestrial subduction one-sided? *Geology* **36**, 43–46.

Gorczyk W., Willner A. P., Gerya T. V., Connolly J. A. D. and Burg J.-P. (2007) Physical controls of magmatic productivity at Pacific-type convergent margins: numerical modelling. *Phys. Earth Planet. Inter.* **163**, 209–232.

Goren L., Aharonov E., Mulugeta G., Koyi H. A. and Mart Y. (2008) Ductile deformation of passive margins: a new mechanism for subduction initiation. *J. Geophys. Res.* **113**, B08411.

Gray C. M. (1984) An isotopic mixing model for the origin of granitic rocks in Southeastern Australia. *Earth Planet. Sci. Lett.* **70**, 47–60.

Gray C. M. (1990) A strontium isotopic traverse across the granitic rocks of Southeastern Australia: petrogenetic and tectonic implications. *Aust. J. Earth Sci.* **37**, 331–349.

Griffin W. L., Pearson N. J., Belousova E., Jackson S. E., van Achterbergh E., O'Reilly S. Y. and Shee S. R. (2000) The Hf isotope composition of cratonic mantle: LA-MC-ICPMS analysis of zircon megacrysts in kimberlites. *Geochim. Cosmochim. Acta* **64**, 133–147.

Hall C. E., Gurnis M., Sdrolias M., Lavier L. L. and Müller R. D. (2003) Catastrophic initiation of subduction following forced convergence across fracture zones. *Earth Planet. Sci. Lett.* **212**, 15–30.

Hanchar J. M. and Watson E. B. (2003) Zircon saturation thermometry. *Rev. Mineral. Geochem.* **53**, 89–112.

Harrison T. M., Lovera O. M. and Grove M. (1997) New insights into the origin of two contrasting Himalayan granite belts. *Geology* **25**, 899–902.

Healy B., Collins W. J. and Richards S. W. (2004) A hybrid origin for Lachlan S-type granites: the Murrumbidgee Batholith example. *Lithos* **78**, 197–216.

Hou K. J., Li Y. H., Zou T. R., Qu X. M., Shi Y. R. and Xie G. Q. (2007) Laser ablation-MC-ICP-MS technique for Hf isotope microanalysis of zircon and its geological applications. *Acta Petrol. Sin.* **23**, 2595–2604.

Inger S. and Harris N. (1993) Geochemical constraints on leucogranite magmatism in the Langtang Valley, Nepal Himalaya. *J. Petrol.* **34**, 345–368.

Ishizuka O., Tani K., Reagan M. K., Kanayama K., Umino S., Harigane Y., Sakamoto I., Miyajima Y., Yuasa M. and Dunkley D. J. (2011) The timescales of subduction initiation

and subsequent evolution of an oceanic island arc. *Earth Planet. Sci. Lett.* **306**, 229–240.

Jahn B. M., Cornichet J., Cong B. L. and Yui T. F. (1996) Ultrahigh-εNd eclogites from an ultrahigh-pressure metamorphic terrane of China. *Chem. Geol.* **127**, 61–79.

Keay S., Collins W. J. and McCulloch M. T. (1997) A three-component Sr–Nd isotopic mixing model for granitoid genesis, Lachlan fold belt, eastern Australia. *Geology* **25**, 307–310.

Li X. H., Li Z. X., Ge W. C., Zhou H. W., Li W. X., Liu Y. and Wingate M. T. D. (2003) Neoproterozoic granitoids in South China: crustal melting above a mantle plume at ca. 825 Ma? *Precambr. Res.* **122**, 45–83.

Li X. H., Liu Y., Li Q. L. and Guo C. H. (2009) Precise determination of Phanerozoic zircon Pb/Pb age by multicollector SIMS without external standardization. *Geochem. Geophys. Geosyst.* **10**, Q04010. http://dx.doi.org/10.1029/2009GC002400.

Lucassen F., Trumbull R., Franz G., Creixell C., Vásquez P., Romer R. L. and Figueroa O. (2004) Distinguishing crustal recycling and juvenile additions at active continental margins: the Paleozoic to recent compositional evolution of the Chilean Pacific margin (36–41°S). *J. S. Am. Earth Sci.* **17**, 103–119.

Ludwig K. R. (2003) User's manual for isoplot 3.0: a geochronological toolkit for Microsoft excel. *Berkeley Geochronol. Centre Spec. Publ.* **4**, 1–71.

Maas R., Nicholls I. A., Greig A. and Nemchin A. (2001) U–Pb zircon studies of mid-crustal metasedimentary enclaves from the S-type Deddick granodiorite, Lachlan fold belt, SE Australia. *J. Petrol.* **42**, 1429–1448.

Mart Y., Aharonov E., Mulugeta G., Ryan W., Tentler T. and Goren L. (2005) Analogue modelling of the initiation of subduction. *Geophys. J. Int.* **160**, 1081–1091.

McCulloch M. T. and Chappell B. W. (1982) Nd isotopic characteristics of S- and I-type granites. *Earth Planet. Sci. Lett.* **58**, 51–64.

Miller C. F. (1985) Are strongly peraluminous magmas derived from pelitic sedimentary sources? *J. Geol.* **93**, 673–689.

Miller C. F., McDowell S. M. and Mapes R. W. (2003) Hot and cold granites? Implications of zircon saturation temperatures and preservation of inheritance. *Geology* **31**, 529–532.

Montel J. M. and Vielzeuf D. (1997) Partial melting of metagreywackes, Part II. Compositions of minerals and melts. *Contrib. Miner. Petrol.* **128**, 176–196.

Morel M. L. A., Nebel O., Nebel-Jacobsen Y. J., Miller J. S. and Vroon P. Z. (2008) Hafnium isotope characterization of the GJ-1 zircon reference material by solution and laser-ablation MC-ICPMS. *Chem. Geol.* **255**, 231–235.

Nikolaeva K., Gerya T. V. and Connolly J. A. D. (2008) Numerical modelling of crustal growth in intraoceanic volcanic arcs. *Phys. Earth Planet. Inter.* **171**, 336–356.

Nikolaeva K., Gerya T. V. and Marques F. O. (2010) Subduction initiation at passive margins: numerical modeling. *J. Geophys. Res.* **115**, B03406.

Nikolaeva K., Gerya T. V. and Marques F. O. (2011) Numerical analysis of subduction initiation risk along the Atlantic American passive margins. *Geology* **39**, 463–466.

Niu Y. L., O'Hara M. J. and Pearce J. A. (2003) Initiation of subduction zones as a consequence of lateral compositional buoyancy contrast within the lithosphere: a petrological perspective. *J. Petrol.* **44**, 851–866.

Patiño Douce A. E. (1995) Experimental generation of hybrid silicic melts by reaction of high-Al basalt with metamorphic rocks. *J. Geophys. Res.* **100**, 15623–15639.

Patiño Douce A. E. (1999) What do experiments tell us about the relative contributions of crust and mantle to the origin of granitic magmas? *Geol. Soc. London Spec. Publ.* **168**, 55–75.

Patiño Douce A. E. and Beard J. S. (1995) Dehydration-melting of biotite gneiss and quartz amphibolite from 3 to 15 kbar. *J. Petrol.* **36**, 707–738.

Patiño Douce A. E. and Harris N. (1998) Experimental constraints on Himalayan anatexis. *J. Petrol.* **39**, 689–710.

Patiño Douce A. E. and Johnston A. D. (1991) Phase equilibria and melt productivity in the pelitic system: implications for the origin of peraluminous granitoids and aluminous granulites. *Contrib. Miner. Petrol.* **107**, 202–218.

Rollison H. R. (1993) *Using Geochemical Data: Evaluation, Presentation, Interpretation*. Longman Scientific & Technical, p. 162.

Rudnick R. L. and Gao S. (2003) Composition of the continental crust. In *Treatise on Geochemistry* (eds. D. H. Heinrich and K. T. Karl). Pergamon, Oxford, pp. 1–64.

Scherer E., Münker C. and Mezger K. (2001) Calibration of the Lutetium-Hafnium clock. *Science* **293**, 683–687.

Searle M. P. and Fryer B. J. (1986) Garnet, tourmaline and muscovite-bearing leucogranites, gneisses and migmatites of the Higher Himalayas from Zanskar, Kulu, Lahoul and Kashmir. *Geol. Soc. London Spec. Publ.* **19**, 185–201.

Shau Y. H., Yang H. Y. and Peacor D. R. (1991) On oriented titanite and rutile inclusions in sagenitic biotite. *Am. Mineral.* **76**, 1205–1217.

Shaw S. E., Todd V. R. and Grove M. (2003) Jurassic peraluminous gneissic granites in the axial zone of the Peninsular Ranges, southern California. *Geol. Soc. Am. Spec. Pap.* **374**, 157–183.

Shi R. D., Yang J. S., Wu C. L. and Wooden J. (2004) First SHRIMP dating of the formation of the Late Sinian Yushigou ophiolite, North Qilian Mountains. *Acta Geol. Sinica* **78**, 649–657.

Skjerlie K. P., Patiño Douce A. E. and Johnston A. D. (1993) Fluid absent melting of a layered crustal protolith: implications for the generation of anatectic granites. *Contrib. Miner. Petrol.* **114**, 365–378.

Song S. G., Zhang L. F., Niu Y. L., Su L., Song B. and Liu D. Y. (2006) Evolution from oceanic subduction to continental collision: a case study from the northern Tibetan Plateau based on geochemical and geochronological data. *J. Petrol.* **47**, 435–455.

Song S. G., Zhang L. F., Niu Y., Wei C. J., Liou J. G. and Shu G. M. (2007) Eclogite and carpholite-bearing metasedimentary rocks in the North Qilian suture zone, NW China: implications for Early Palaeozoic cold oceanic subduction and water transport into mantle. *J. Metamorph. Geol.* **25**, 547–563.

Song S. G., Niu Y. L., Zhang L. F., Wei C. J., Liou J. G. and Su L. (2009a) Tectonic evolution of early Paleozoic HP metamorphic rocks in the North Qilian Mountains, NW China: new perspectives. *J. Asian Earth Sci.* **35**, 334–353.

Song S. G., Su L., Niu Y. L., Lai Y. and Zhang L. F. (2009b) CH4 inclusions in orogenic harzburgite: evidence for reduced slab fluids and implication for redox melting in mantle wedge. *Geochim. Cosmochim. Acta* **73**, 1737–1754.

Song S. G., Niu Y. L., Wei C. J., Ji J. Q. and Su L. (2010a) Metamorphism, anatexis, zircon ages and tectonic evolution of the Gongshan block in the northern Indochina continent – an eastern extension of the Lhasa Block. *Lithos* **120**, 327–346.

Song S. G., Su L., Li X. H., Zhang G. B., Niu Y. L. and Zhang L. F. (2010b) Tracing the 850-Ma continental flood basalts from a piece of subducted continental crust in the North Qaidam UHPM belt, NW China. *Precambr. Res.* **183**, 805–816.

Song S. G., Niu Y. L., Su L. and Xia X. H. (2013) Tectonics of the North Qilian orogen, NW China. *Gondwana Res.* **23**, 1378–1401.

Stevens G., Villaros A. and Moyen J. F. (2007) Selective peritectic garnet entranment as the origin of geochemical diversity in S-type granites. *Geology* **35**, 9–12.

Su J. P., Hu N. G., Zhang H. F. and Fu G. M. (2004) Single-zircon U–Pb dating and geological significance of the Diaodaban granitic gneiss in the western segment of the North Qilian Mountain. *Geol. Sci. Technol. Inf.* **23**, 11–14.

Sun S. S. and McDonough W. F. (1989) Chemical and isotopic systematics of oceanic basalts: implications for mantle composition and processes. *Geol. Soc. London Spec. Publ.* **42**, 313–345.

Sylvester P. J. (1998) Post-collisional strongly peraluminous granites. *Lithos* **45**, 29–44.

Tseng C. Y., Yang H. Y., Wan Y. S., Dunyi L., Wen D. J., Lin T. C. and Tung K. A. (2006) Finding of Neoproterozoic (~775 Ma) magmatism recorded in metamorphic complexes from the North Qilian orogen: evidence from SHRIMP zircon U–Pb dating. *Chin. Sci. Bull.* **51**, 963–970.

Tseng C. Y., Yang H. J., Yang H. Y., Liu D. Y., Tsai C. L., Wu H. Q. and Zuo G. C. (2007) The Dongcaohe ophiolite from the North Qilian Mountains: a fossil oceanic crust of the Paleo-Qilian ocean. *Chin. Sci. Bull.* **52**, 2390–2401.

Tseng C. Y., Yang H. J., Yang H. Y., Liu D. Y., Wu C. L., Cheng C. K., Chen C. H. and Ker C. M. (2009) Continuity of the North Qilian and North Qinling orogenic belts, Central Orogenic System of China: evidence from newly discovered Paleozoic adakitic rocks. *Gondwana Res.* **16**, 285–293.

Vernon R. H. (2007) Problems in identifying restite in S-type granites of Southeastern Australia, with speculations on sources of magma and enclaves. *Can. Mineral.* **45**, 147–178.

Vielzeuf D. and Holloway J. R. (1988) Experimental determination of the fluid-absent melting relations in the pelitic system. *Contrib. Miner. Petrol.* **98**, 257–276.

Vielzeuf D. and Montel J. M. (1994) Partial melting of metagreywackes. Part I. Fluid-absent experiments and phase relationships. *Contrib. Miner. Petrol.* **117**, 375–393.

Wang C. Y., Zhang Q. and Qian Q. (2005) Geochemistry of the Early Paleozoic Baiyin volcanic rocks (NW China): implications for the tectonic evolution of the North Qilian orogenic belt. *J. Geol.* **113**, 83–94.

Watson E. B. and Harrison T. M. (1983) Zircon saturation revisited: temperature and composition effects in a variety of crustal magma types. *Earth Planet. Sci. Lett.* **64**, 295–304.

Watson E. B. and Harrison T. M. (2005) Zircon thermometer reveals minimum melting conditions on earliest Earth. *Science* **308**, 841–844.

White A. J. R., Chappell B. W. and Wyborn D. (1999) Application of the restite model to the Deddick Granodiorite and its enclaves – a reinterpretation of the observations and data of Maas et al. (1997). *J. Petrol.* **40**, 413–421.

Wiedenbeck M., AllÉ P., Corfu F., Griffin W. L., Meier M., Oberli F., Quadt A. V., Roddick J. C. and Spiegel W. (1995) Three natural zircon standards for U–Th–Pb, Lu–Hf, trace element and REE analyses. *Geostand. Newsl.* **19**, 1–23.

Williamson B. J., Shaw A., Downes H. and Thirlwall M. F. (1996) Geochemical constraints on the genesis of Hercynian two-mica leucogranites from the Massif Central, France. *Chem. Geol.* **127**, 25–42.

Wu H. Q., Feng Y. M. and Song S. G. (1993) Metamorphism and deformation of blueschist belts and their tectonic implications, North Qilian Mountains, China. *J. Metamorph. Geol.* **11**, 523–536.

Wu F. Y., Jahn B. M., Wilde S. A., Lo C. H., Yui T. F., Lin Q., Ge W. C. and Sun D. Y. (2003a) Highly fractionated I-type granites in NE China (I): geochronology and petrogenesis. *Lithos* **66**, 241–273.

Wu F. Y., Jahn B. M., Wilde S. A., Lo C. H., Yui T. F., Lin Q., Ge W. C. and Sun D. Y. (2003b) Highly fractionated I-type granites in NE China (II): isotopic geochemistry and implications for crustal growth in the Phanerozoic. *Lithos* **67**, 191–204.

Wu C. L., Yao S. Z., Yang J. S., Zeng L. S., Chen S. Y., Li H. B., Qi X. X., Wooden J. L. and Mazdab F. K. (2006a) Double subduction of the Early Paleozoic North Qilian oceanic plate: evidence from granites in the central segment of North Qilian, NW China. *Geol. China* **33**, 1197–1208.

Wu F. Y., Yang Y. H., Xie L. W., Yang J. H. and Xu P. (2006b) Hf isotopic compositions of the standard zircons and baddeleyites used in U–Pb geochronology. *Chem. Geol.* **234**, 105–126.

Wu Y. B., Zheng Y. F., Zhang S. B., Zhao Z. F., Wu F. Y. and Liu X. M. (2007). *Zircon U–Pb ages and Hf isotope compositions of migmatite from the North Dabie terrane in China: constraints on partial melting* **25**, 991–1009.

Wu C. L., Xu X. Y., Gao Q. M., Li X. M., Lei M., Gao Y. H., Forst R. B. and Wooden J. L. (2010) Early Paleozoic granitoid magmatism and tectonic evolution in North Qilian, NW China. *Acta Petrol. Sinica* **26**, 1027–1044.

Wu C. L., Gao Y. H., Frost B. R., Robinson P. T., Wooden J. L., Wu S. P., Chen Q. L. and Lei M. (2011) An early Palaeozoic double-subduction model for the North Qilian oceanic plate: evidence from zircon SHRIMP dating of granites. *Int. Geol. Rev.* **53**, 157–181.

Xia X. H. (2012) *Study on the Earliest Stage of Arc Magmatic Activity and Back-arc Basin Development in the North Qilian Orogenic Belt*. Peking University.

Xia X. H. and Song S. G. (2010) Forming age and tectonopetrogenises of the Jiugequan ophiolite in the North Qilian Mountain, NW China. *Chin. Sci. Bull.* **55**, 1899–1907.

Xia L. Q., Xia Z. C. and Xu X. Y. (2003) Magmagenesis in the Ordovician backarc basins of the Northern Qilian Mountains, China. *Geol. Soc. Am. Bull.* **115**, 1510–1522.

Xia X. H., Song S. G. and Niu Y. L. (2012) Tholeiite-Boninite terrane in the North Qilian suture zone: implications for subduction initiation and back-arc basin development. *Chem. Geol.* **328**, 259–277.

Xiao X. C., Chen G. M. and Zhu Z. Z. (1978) A preliminary study on the tectonics ancient ophiolites in the Qilian Mountains, Northwest China. *Acta Geol. Sinica* **52**, 281–295.

Xu W. C. (2007) U–Pb zircon geochronology, geochemical and Sr–Nd–Pb isotopic compositions of the Hualong group in Qilian Mountains: constraints on tectonic evolution of crust. Ph. D. thesis, China University of Geosciences. p. 150.

Xu Y. J., Du Y. S., Cawood P. A., Guo H., Huang H. and An Z. H. (2010) Detrital zircon record of continental collision: assembly of the Qilian orogen, China. *Sed. Geol.* **230**, 35–45.

Yang J. H., Wu F. Y., Wilde S., Xie L. W., Yang Y. H. and Liu X. M. (2007) Tracing magma mixing in granite genesis: in situ U–Pb dating and Hf-isotope analysis of zircons. *Contrib. Miner. Petrol.* **153**, 177–190.

Yang J. H., Du Y. S., Cawood P. A. and Xu Y. J. (2009) Silurian collisional suturing onto the southern margin of the North China craton: detrital zircon geochronology constraints from the North Qilian orogen. *Sed. Geol.* **220**, 95–104.

Zhang J. X., Xu Z. Q., Chen W. and Xu H. F. (1997) A tentative discussion on the ages of the subduction-accretionary complex/volcanic arcs in the middle sector of North Qilian Mountain. *Acta Petrol. Mineral.* **16**, 17–24.

Zhang Q., Chen Y., Zhou D., Qian Q., Jia X. and Han S. (1998) Geochemical characteristics and genesis of Dachadaban ophiolite in North Qilian area. *Sci. China, Ser. D Earth Sci.* **41**, 277–281.

Zhang J. X., Zhang Z. M., Xu Z. Q., Yang J. S. and Cui J. W. (2001) Petrology and geochronology of eclogites from the

western segment of the Altyn Tagh, northwestern China. *Lithos* **56**, 187–206.

Zhang J. X., Meng F. C. and Wan Y. S. (2007) A cold Early Palaeozoic subduction zone in the North Qilian Mountains, NW China: petrological and U–Pb geochronological constraints. *J. Metamorph. Geol.* **25**, 285–304.

Zhu G., Gerya T. V., Yuen D. A., Honda S., Yoshida T. and Connolly J. A. D. (2009) Three-dimensional dynamics of hydrous thermal-chemical plumes in oceanic subduction zones. *Geochem. Geophys. Geosyst.* **10**, Q11006.

Zou H. B. (2007) *Quantitative Geochemistry*. Imperial College Press, London, pp. 115–117.

Associate editor: Weidong Sun